Palaeogeography, Palaeoclimatology, Palaeoecology 545 (2020) 109653

Contents lists available at ScienceDirect

Palaeogeography, Palaeoclimatology, Palaeoecology

journal homepage: www.elsevier.com/locate/palaeo

Paleo-environmental variation and its control on organic matter enrichment of black shales from shallow shelf to slope regions on the Upper Yangtze Platform during Cambrian Stage 3

Yaowen Wu[a,b], Hui Tian[a,*], Dajian Gong[c], Tengfei Li[a], Qin Zhou[a]

[a] State Key Laboratory of Organic Geochemistry, Guangzhou Institute of Geochemistry, Chinese Academy of Sciences, Guangzhou 510640, China
[b] University of Chinese Academy of Science, Beijing 100049, China
[c] Tongren Zhongneng Natural Gas Co., Ltd., Tongren 554300, China

ARTICLE INFO

Editor: Thomas Algeo

Keywords:
South China
Hydrothermal activity
Primary productivity
Redox conditions
Hyalophane

ABSTRACT

To understand the evolution of oceanic redox conditions and organic matter (OM) accumulation in the shelf and slope regions of the Upper Yangtze Platform during Cambrian Stage 3, high-resolution geochemical data were obtained from two wells respectively representing shelf and slope environments. Based on redox proxies, widespread anoxic/euxinic waters with intermittent sulfidic water columns were formed from shallow shelf to deep water slope and basinal regions during Stage 2 and early Stage 3; then, widespread anoxic waters were reduced and oxic waters expanded during the middle Stage 3, after which fluctuating suboxic and oxic (occasionally anoxic) environments became predominant during late Stage 3. The presence of hyalophane and positive Eu anomalies suggest strong Ba-rich hydrothermal activities in the shelf and deep basin regions during early and middle Stage 3. The Ba-rich hydrothermal fluids and upwelling events enhanced the primary productivity in surface waters and subsequently promoted organic matter enrichment. During Stage 2 and early Stage 3, the high primary productivity driven by coastal upwelling and hydrothermal activity were the main factors controlling OM enrichment; during middle Stage 3, the local anoxic water condition became responsible for OM enrichment when oxic waters began to gradually expand; during late Stage 3, both primary productivity and redox conditions became the main control factors for OM enrichment. According to the analysis of primary productivity, redox conditions, hydrothermal activity and upwelling events, an evolution model is proposed to account for the paleo-environmental variation and the OM enrichment from shallow shelf to slope regions during Cambrian Stage 3.

1. Introduction

The Ediacaran-Cambrian (E–C) transition was a critical time in Earth history and many global environmental and biological change events occurred at the time, including the stepwise oxygenation of the global ocean and subsequent Cambrian radiation of animals (Amthor et al., 2003; Kimura and Watanabe, 2001; Knoll and Carroll, 1999; Marshall, 2006). Several lines of previous geochemical studies suggest that the evident oxygenation of global ocean basins may have taken place in the late Ediacaran and triggered the subsequent "Cambrian Explosion" (Canfield et al., 2007; X. Chen et al., 2015; Fike et al., 2006; Li et al., 2017; Scott et al., 2008). However, more geochemical proxies provide evidence for the persistence of anoxic/ferruginous deeper waters across the Ediacaran-Cambrian transition, particularly in the Yangtze Block of South China (Canfield et al., 2008; Goldberg et al., 2007; Och et al., 2013; Pi et al., 2013; Wang et al., 2012), which apparently conflicts with the theory of immediate oceanic oxygenation. The widespread black shale successions on the Yangtze Block in South China are characterized by a set of chert, phosphorite, abundant biofossils and even unusual Ni-Mo polymetallic ore layers and thus provide a unique opportunity to study the oceanic environmental changes at this critical period of Earth history (Chen et al., 2009; Gao et al., 2018; G. Jiang et al., 2007; S.Y. Jiang et al., 2007b; Jin et al., 2016; Pi et al., 2013; Y. Zhang et al., 2017).

Early Cambrian ocean on the Yangtze Platform in South China has been well studied with respect to ocean redox (Goldberg et al., 2007; Lehmann et al., 2007; Li et al., 2018; D. Wang et al., 2015; Wang et al., 2012; Xu et al., 2012), hydrothermal activities and upwelling events (Chen et al., 2009; Gao et al., 2018; S.Y. Jiang et al., 2007a; Li et al., 2015; Liu et al., 2015; Lott et al., 1999; Yeasmin et al., 2017). Previous

* Corresponding author at: #511 Kehua Road, Tianhe District, Guangzhou City, Guangdong Province, China.
E-mail address: tianhui@gig.ac.cn (H. Tian).

https://doi.org/10.1016/j.palaeo.2020.109653
Received 12 November 2019; Received in revised form 7 February 2020; Accepted 7 February 2020
Available online 12 February 2020
0031-0182/

studies suggested that organic-rich black shales were deposited under anoxic to euxinic conditions due to global transgression during the early Cambrian (Feng et al., 2014; Guo et al., 2007; Lehmann et al., 2007; Och et al., 2013; Pi et al., 2013; Wang et al., 2012). The enrichment of organic matter (OM) in this succession of shales may be ascribed to (1) high primary productivity (Yeasmin et al., 2017); (2) a high sea level and low sedimentation rate due to a rapid transgression at the beginning of the Cambrian Period (Wang et al., 2013); (3) an upwelling event around the slope region (Xia et al., 2015; Yeasmin et al., 2017); (4) hydrothermal activity in local areas (Liu et al., 2015; K. Zhang et al., 2017; Zhang et al., 2019); as well as (5) being an anoxic sedimentary environment (Gao et al., 2016; Han et al., 2013; S. Wang et al., 2015; Zhang et al., 2019; Y. Zhang et al., 2017). All these results indicate that the OM enrichment in the Lower Cambrian shales is likely controlled by multiple geological and geochemical processes which may vary in different sedimentary environments.

Most early studies hold a viewpoint of widespread anoxic ocean, especially in the deep ocean, during early Cambrian (Feng et al., 2014; Jiang et al., 2009; Pi et al., 2014; Wang et al., 2012), which apparently conflicts with an expected increase of ocean oxygenation immediately during the latest Cambrian Stage 2 (ca. 521 Ma) (X. Chen et al., 2015). Therefore, more work is needed to trace the stepwise expansion of oxygenated deep waters across the Yangtze Block during early Cambrian in different sedimentary environments. At the same time, most studies are focused on the influence of hydrothermal activity on the formation of the Ni-Mo polymetallic ore layer during Cambrian Stage 2 (Chen et al., 2006; Gao et al., 2018; Han et al., 2015; S.Y. Jiang et al., 2007a; Lott et al., 1999; Steiner et al., 2001; Wang et al., 2012), and less attention has been paid to the influence of hydrothermal activity on OM enrichment in black shales during Cambrian Stage 3.

In the present study, core samples of Lower Cambrian shales were collected from a GMD-1 well of shelf region and a TX-1 well of slope region for geochemical analyses. The main objectives of this study are to (1) investigate changes in the primary productivity, redox conditions, and hydrothermal activity and trace the stepwise oxygenation from shallow shelf to slope regions during Cambrian Stage 3; (2) reconstruct the paleo-environmental variations and multiple controls on OM enrichment of black shales.

2. Geological setting

The Upper Yangtze Platform is bounded by the Qinling-Dabie orogenic belt to the north, the Red River Fault Zone to the southwest, the Xianshuihe Fault Zone to the west, and the Cathaysia Platform to the southeast (Shu, 2012). During the E–C transition, the Upper Yangtze Platform evolved from a rift basin to a passive continental margin basin, and carbonate platform facies prevailed in most parts of the Yangtze Platform (Wang and Li, 2003). Following the northwestward transgression during the Early Cambrian, the sedimentary facies changed from shallow water carbonate facies in the platform interior, through transitional facies, to the deep water slope and basin facies in the southeast region (Chen et al., 2009; Gao et al., 2018; Steiner et al., 2001) (Fig. 1). As a result of large-scale marine transgression, organic-rich black shales were widely formed from shallow shelf to deep water slope and basin regions across the whole Yangtze Platform during the early Cambrian (Feng et al., 2014). A diagnostic polymetallic Ni–Mo–PGE–Au sulfide ore layer developed at the bottom of the Lower Cambrian Niutitang Formation both in the transitional and deep basin facies (S.Y. Jiang et al., 2007a; Xu et al., 2013). In addition, barite deposits are also identified in the Lower Cambrian Niutitang Formation where deep faults are present (Chen et al., 2009; Han et al., 2015).

The GMD-1 well (27°44′01″N and 107°30′35″E) in the shelf region and the TX-1 well (27°24′32″N and 108°51′40″E) in the slope region were selected for detailed geochemical analyses (Fig. 1). The GMD-1 well is located in the northwest of Meitan County, ~165 km northeast of Guiyang City in Guizhou Province, while the TX-1 well is located in southeastern Cengong County, ~230 km east of Guiyang City in Guizhou Province (Fig. 1). The Niutitang Formation of the GMD-1 well is approximately 140 m thick, and the thickness of the Niutitang Formation of the TX-1 well is approximately 70 m. The sedimentary successions penetrated by the GMD-1 well include the dolomite-dominated Ediacaran Dengying Formation, the Cambrian Niutitang Formation that unconformably overlies on the Dengying Formation and is composed mainly of cherty shale, phosphorite, the Ni-Mo polymetallic ore layer, carbonaceous shale, and silty shale (from bottom to top) (Fig. 2). The TX-1 well penetrated the Ediacaran-Cambrian Liuchapo Formation consisting mostly of chert, the Cambrian Niutitang Formation that conformably overlaid on the Liuchapo Formation and is mainly composed of phosphorite, carbonaceous shales and silty shales (from bottom to top) (Fig. 2).

The E-C boundary is defined by the existence of small shelly faunas, and a U-Pb age of 542 ± 0.3 Ma has been widely accepted as the start of the Cambrian Period (Amthor et al., 2003). More recently, a new U-Pb age of 542.6 ± 3.7 Ma was measured from the Bahuang Liuchapo chert formation in the slope region, which approximates the E–C boundary age (D. Chen et al., 2015) (Fig. 2). Jiang et al. (2009) reported a U-Pb zircon age of 532.3 ± 0.7 Ma for a volcanic ash bed at the bottom of the Niutitang Formation in the Zhongnancun section (Fig. 2). Considering that the Ni-Mo polymetallic ore layer is present in the lowermost part of the Niutitang Formation with a thickness mostly of 3 to 5 cm, it can act as a marker for lithostratigraphic correlation of the Cambrian sedimentary rocks. Samples from the Ni-Mo polymetallic ore layer in the Zhongnan section in the shelf facies yield a Re-Os age of 521 ± 5 Ma, which is consistent with a Tommotian or late Meishucunian biostratigraphic age (Xu et al., 2011); D. Chen et al. (2015) also reported a U-Pb age of 522.3 ± 3.7 Ma for the Bahuang phosphorite at the bottom of the Niutitang Formation in the slope facies, which is consistent with the Re-Os age of the Ni-Mo polymetallic ore layer in the shelf region. Therefore, the Ni-Mo layer may be treated as the approximate boundary of Stage 2 and Stage 3 in the study area (Fig. 2). In addition, the small shelly fossil assemblages 1 to 3 (SSFs1–3) were found widely in the shallow shelf region above the Ediacaran Dengying Formation in South China, and considered to be formed during Cambrian Fortunian and Stage 2 (ca. 542–521) (Steiner et al., 2007; Zhu et al., 2003). However, SSFs-containing strata are absent in the outer shelf and slope regions (including GMD-1 and TX-1 wells) due to stratigraphic unconformity at the boundary of Ediacaran and Cambrian (Fig. 2), and therefore the appearance of Trilobite fossils was commonly used to define the Cambrian Stage 3 (ca. 521–514 Ma) (Babcock et al., 2005). The Trilobite fossils were found in the silty shales of Niutitang Formation in the shallow shelf region at Jinsha section, ~50 km southwest from GMD-1 well and corresponding to the similar silty shales in the upper part of Niutitang Formation (Yang et al., 2014) and the silty shales and muddy limestone at the Songtao section, ~60 km northeast from TX-1 well and corresponding to the upper part of Niutitang Formation (Zhao et al., 2001). The bio-stratigraphic records and radiometric ages jointly suggest that the black shale sequence was likely formed during Stages 2 and 3 (ca. 529–514 Ma) of early Cambrian (Feng et al., 2014).

In this study, the Niutitang Formation can be subdivided into three units, i.e., the lower, middle and the upper units (Fig. 2). The lower unit (20–74 m) is dominated by carbonaceous shales with cherty shale and phosphatic nodules; the middle unit is thin (ca. 3–5 m) and characterized by Ni, Mo and U enrichments, and the upper unit (32–35 m) is mainly composed of interbedded mudstones and silty mudstones. Based on the lithostratigraphic and biostratigraphic data in the study area (Amthor et al., 2003; D. Chen et al., 2015; Xu et al., 2011; Y. Zhang et al., 2017), the lower unit was formed from Stage 2 to early Stage 3, the middle unit during middle Stage 3, and the upper unit during late Stage 3.

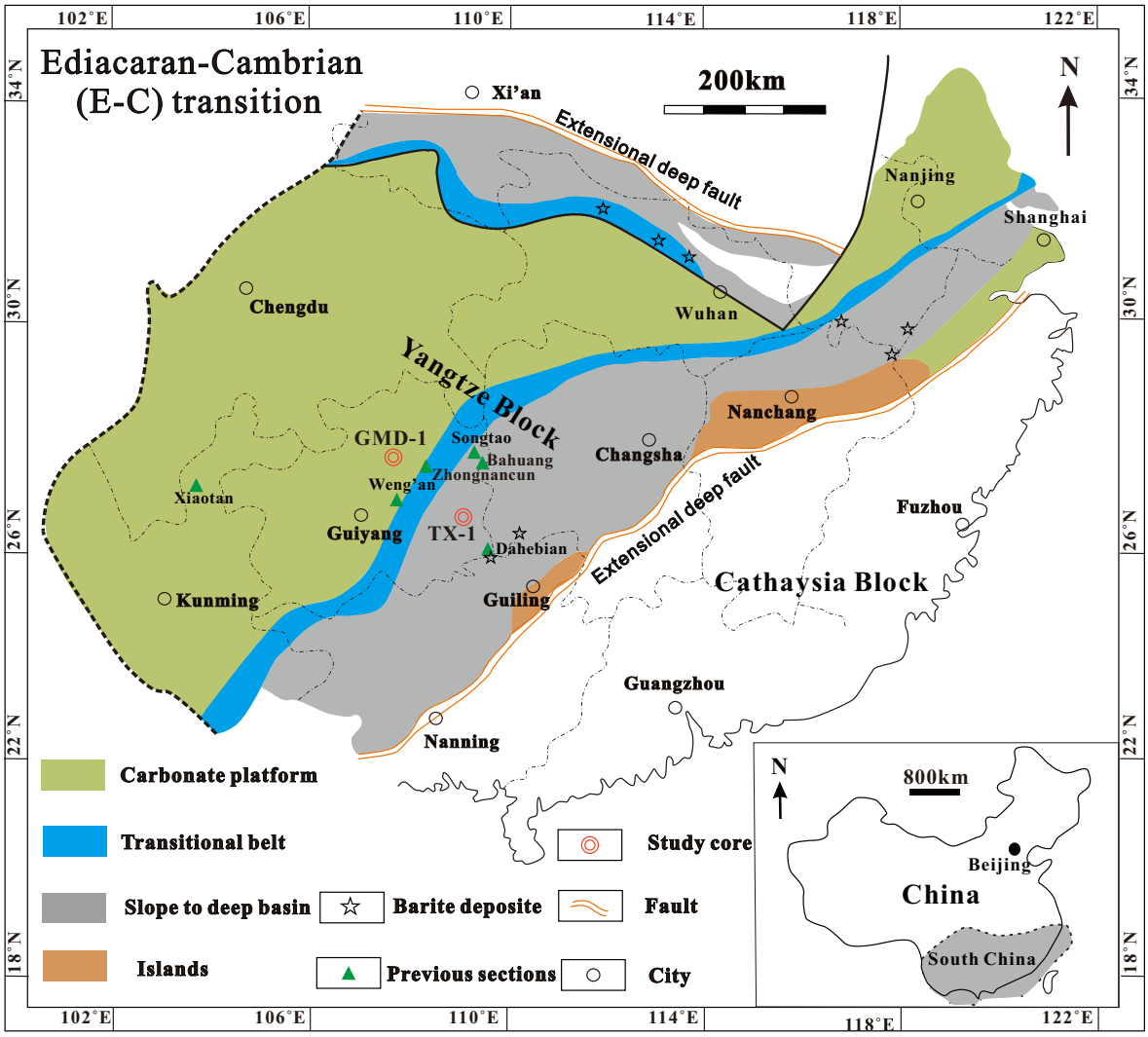

Fig. 1. Simplified paleogeographic map showing the Yangtze Block during the E-C transition.
(Modified after Chen et al. (2009) and Gao et al. (2018).)

3. Samples and methods

3.1. Samples

Based on the lithology and strata thickness, 126 core samples from the GMD-1 well and 41 samples from the TX-1 well were collected for TOC analysis; in terms of the TOC results, 44 samples from the GMD-1 well and 17 samples from the TX-1 well were subjected to elemental analysis.

3.2. TOC, microscopic and FE-SEM observation

Measurements of total organic carbon (TOC) content were conducted on a Leco CS230 carbon/sulfur analyzer after samples were treated with 6 mol/L diluted hydrochloric acid solution (HCl) to remove carbonates. Microscopic observation of polished thin sections was performed on a Leica DM2500P microscope. Scanning electron microscopy observation was completed via high-resolution field emission scanning electron microscopy (FE-SEM, Hitachi S-8000) equipped with an energy dispersive spectrometer (EDS) instrument. To obtain a highly smooth surface, samples were polished with an argon ion milling system IM4000. The working distance for FE-SEM observation was 3.8–4 mm, and the voltage was 1.5 kV. The EDS analysis of some minerals was conducted under backscatter mode with a working distance of 15 mm and a voltage of 15 kV.

3.3. Major, trace and rare earth elements

Fragments of core samples were ground into ca. 200 mesh size with agate mortar. About 1200 mg of powdered samples were oxidized at 900 °C for 3 h, and then mixed with $Li_2B_4O_7$ at a 1:8 ratio. The mixture was melted at about 1200 °C to form fusion glasses and then major oxides of powdered samples were determined by X-ray fluorescence spectrometry (XRF, Philips PW2404) on these fusion glasses. Concentrations of trace and rare earth elements were measured with inductively coupled plasma mass spectrometry (ICP-MS, Thermo Scientific Element XR). About 40 mg of powdered samples (200 mesh) were digested with a mixture of HNO_3 + HCl + HF + $HClO_4$ in high-pressure Teflon cups. To completely remove organic matter before dissolution by acids, the carbonaceous samples were combusted in a muffle oven at 650 °C for 4 h. The analytical procedures and instrument parameters for trace and rare earth elements have been detailed by Li et al. (2015). The Chinese national standards GSR1 (granite) and GSR3 (basalt) plus replicate samples were used to monitor the accuracy of analytical data. The analytical precision was generally better than 7% for trace elements and 10% for rare earth elements, as checked by international standards and analysis of replicate samples. All these analyses were performed at the State Key Laboratory of Isotope

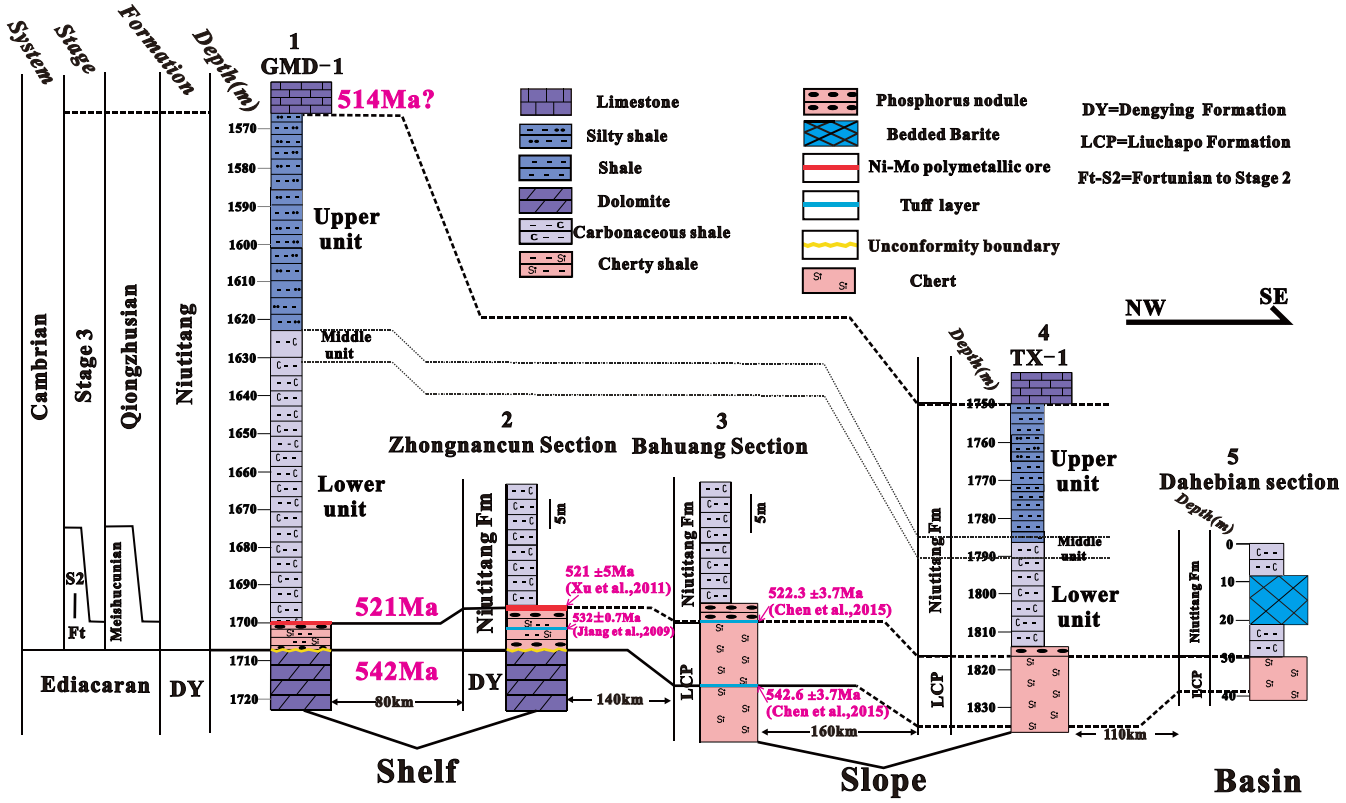

Fig. 2. Lithologic columns of the Cambrian Niutitang Formation shales from shelf to slope and basin regions, including the sampled Well GMD-1 and Well TX-1, Zhongnancun section (Pi et al., 2013), Bahuang section (D. Chen et al., 2015), Dahebian section (Han et al., 2015). The U-Pb ages for Zhongnan and Bahuang sections are from Jiang et al. (2009) and D. Chen et al.(2015). The Re-Os age for Ni-Mo ore of Zhongnan section is from Xu et al. (2011). Locations of these typical sections are shown in Fig. 1.

Geochemistry of Guangzhou Institute of Geochemistry (GIG), Chinese Academy of Sciences (CAS), Guangzhou, China.

Element enrichment factors (EFs) were calculated according to $X_{EF} = [(X / Al)_{sample} / (X / Al)_{PAAS}]$ (Calvert and Pedersen, 1993), where X and Al represent the weight percent values of elements X and Al, and the subscripts of sample and PAAS respectively denote the sample under study and the Post-Archean Australian Shale (PAAS) standard (Taylor and McLennan, 1985). Excess Ba (Ba_{xs}) is assumed to be equivalent to biogenic Ba and calculated as total Ba (Ba_{total}) minus detrital Ba, i.e., $Ba_{xs} = Ba_{total} - (Ba / Al)_{detr} \times Al_{sample}$ (Schoepfer et al., 2015), where $(Ba / Al)_{detr}$ is the ratio of detrital Ba to Al for the PAAS, and Al_{sample} denotes the concentration of Al in the studied samples. Generally, element concentrations are normalized to aluminum (Al) content to diminish the dilution effect (Tribovillard et al., 2006; Van der Weijden, 2002). In this study, element concentrations of the PAAS vs. Al contents were used as the reference for comparison. Cerium (Ce) and europium (Eu) anomalies were calculated according to the formula proposed by Shields and Stille (2001), i.e., $Ce/Ce^* = 3Ce_N / (2La_N + Nd_N)$ and $Eu/Eu^* = Eu_N / (Sm_N \times Gd_N)^{0.5}$, where N refers to elemental concentrations normalized to PAAS (Taylor and McLennan, 1985).

4. Results

4.1. Petrology, mineralogy and organic geochemistry

The lithology of the upper unit is dominated by interbedded black shales and silty gray shales with parallel beddings (Figs. 2 and 3a); the lower unit is composed of organic-rich black shales (Fig. 2). Euhedral to sub-euhedral hyalophane along the cracks and the association of hyalophane, quartz and K-feldspar were identified in the lower unit of the Niutitang Formation in the GMD-1 well (Fig. 3b–f), and the elemental compositions of hyalophane ((K, Ba) $Al_2Si_2O_8$, Frondel et al. (1966)), quartz and K-feldspar were confirmed by EDS spectra (Fig. 4a–c). Han et al. (2015) also reported the presence of hyalophane in the barite deposits in the Dahebian section. Hyalophane is generally associated with barium-rich hydrothermal fluids, and therefore, its presence usually indicates hydrothermal activity (Han et al., 2015; Hou et al., 2001; Kribek et al., 1996).

Pyrite is widely distributed in our samples and is particularly abundant in the lower unit (Fig. 3g). Pyrite is present either as euhedral to sub-euhedral crystals with diameters of 5–18 μm (Figs. 3h and 4d) or as aggregates of framboids with diameters of 2–8 μm (Fig. 3i). The middle unit covers a thickness of several meters (Fig. 2) with calcite fillings (Fig. 3j, k). Ni-Mo polymetallic ore at the basal Niutitang Formation of the GMD-1 well was clearly observed by SEM, consisting largely of a MoSC phase, pyrite, NiS and other metal sulfidic minerals (Figs. 3l and 4e). Sphalerite (ZnS) and chalcopyrite ($CuFeS_2$), indicators of the anoxic/euxinic environment (Morse and Luther, 1999), were also observed in middle unit (Figs. 3n, o, and 4f, g).

Chert nodules surrounded by calcite bands were also observed at the base of the lower unit (Fig. 3m). Phosphate nodules occur locally at the basal Niutitang Formation, and their sizes vary from several millimeters to tens of centimeters, with the majority of them being of centimeter size (Fig. 3p). The phosphate nodules are mainly composed of cryptocrystalline carbonate fluorapatite with the approximate composition of $[Ca_5 (PO_4)_3F]$ (Figs. 3q, r, and 4h).

As shown in Table 1, samples from the GMD-1 well have TOC values varying from 0.7 to 10.7% with an average of 5.2%, and the TOC values for samples from the TX-1 well are in the range of 1.0–6.8% with an average of 2.8%. In general, samples of the lower and middle units have larger TOC values than those of the upper unit (Fig. 2). Microscopic

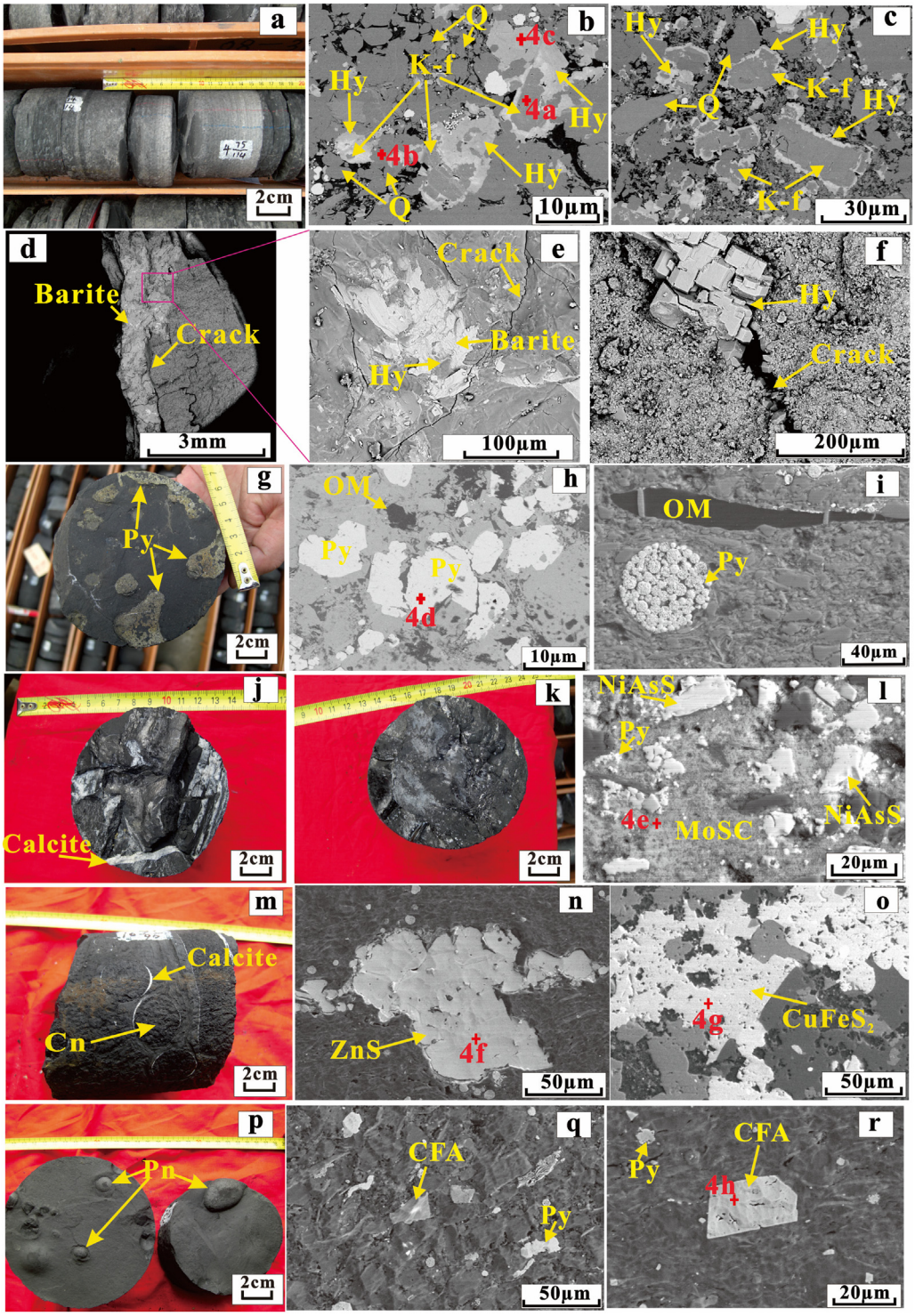

Fig. 3. Photos of representative lithofacies and minerals from the Niutitang Formation. OM = organic matter; Q = quartz; K-f = K-feldspar; Py = pyrite; Hy = hyalophane; Cn = chert nodules; Pn = phosphatic nodules; CFA = carbonate fluorapatite. a: Black shales interbedded with siltstones in the upper Niutitang Formation (GMD-1, 1603.42 m). Note that the horizontal laminations with the presence of local micro-erosive bases in the siltstone interbeds; b: K-feldspar surrounded by Hy (GMD-1, 1659.2 m); c: association of Hy, K–f and Q (GMD-1, 1659.2 m); d: distribution of barite (GMD-1, 1643.9 m); e: hyalophane-containing barite (GMD-1, 1643.9 m); f: idiomorphic-subhedral Hy along cracks (GMD-1, 1630.7 m); g: pyrite along bedding plane in the lower Niutitang Formation (GMD-1, 1603.42 m); h: SEM photography showing massive pyrite and organic matter in the upper Niutitang Formation (GMD-1, 1603.42 m); i: aggregates of framboid pyrites with diameter of 3–9 μm and organic matter bands (GMD-1, 1655.77 m); j: carbonaceous mudstone of the middle unit filled with striped calcite (GMD-1, 1628.18 m); k: carbonaceous mudstone of the middle Unit (TX-1, 1788.57 m); l: SEM electron image of Ni-Mo polymetallic ore in the basal Niutitang Formation (GMD-1, 1699.5 m), consisting of MoSC phase, Py, NiS and other metal sulfidic minerals; m: chert nodules surrounded by calcite rim (GMD-1, 1706.99 m); n: sphalerite (ZnS) with a width of about 80 μm in the middle unit of Well TX-1 (1788.57 m); o: chalcopyrite ($CuFeS_2$) in the middle unit of Well GMD-1 (1630.71 m); p: black shales with abundant phosphatic nodules in the basal Niutitang Formation (TX-1, 1817.14 m); q: photomicrograph of CFA in basal chert (TX-1, 1817.14 m); r: photomicrograph of CFA in basal chert (GMD-1, 1698.88 m). Red cross indicates the location for energy dispersive spectrometer (EDS) analysis and see details in Fig. 4. (For interpretation of the references to color in this figure legend, the reader is referred to the web version of this article.)

examination of kerogen reveals that the organic macerals are dominated by amorphous organic matter (Fig. 5a and b). Strips of organic matter were observed by SEM in whole rock samples (Fig. 5c). Microscopic examination of whole rock also revealed abundant lower aquatic fossils, such as small shelly fossils, sponge needles, and so on (Fig. 5d, e, and f), further indicating that the organic matter in the Cambrian shales is mainly derived from marine algae and other lower aquatic organisms.

4.2. Elemental geochemistry

4.2.1. Major elements

The percentages of selected major elements, expressed as their oxides, are listed in Table 1. For samples from the GMD-1 well, over 80% of the total oxides are composed of SiO_2 (average 63.4%), Al_2O_3 (average 10.7%) and Fe_2O_3 (average 4.2%). The total contents of TiO_2, P_2O_5 and MnO account for < 1% of the total oxides. Generally, the upper unit has a lower content of SiO_2 and higher contents of Al_2O_3 and Fe_2O_3 than the other two units. The content of P_2O_5 is considerably high at the base of the lower unit due to the presence of phosphorus

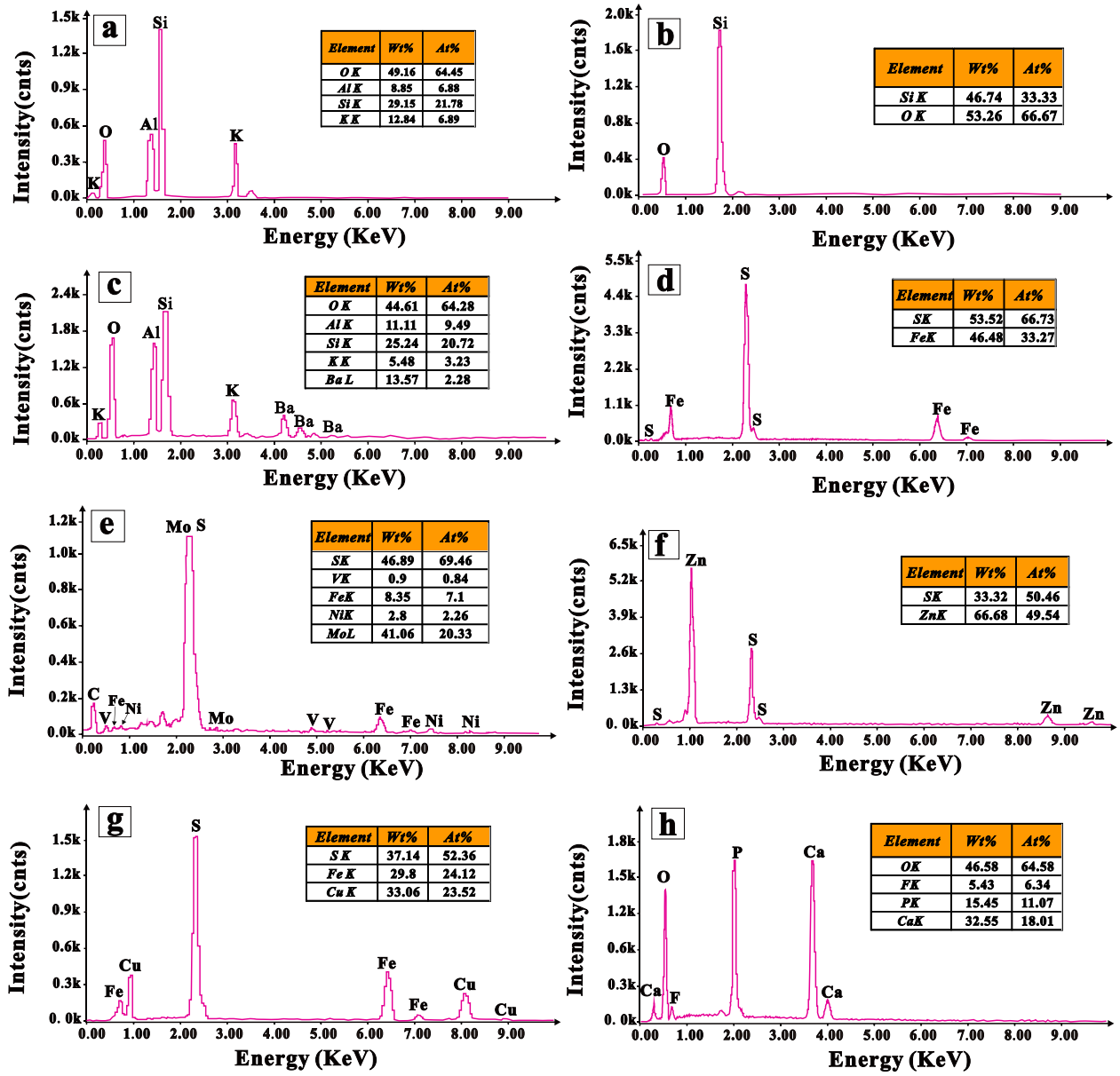

Fig. 4. Energy dispersive spectrometer (EDS) spectra of representative minerals. The numbers of EDS spectra are indicated in Fig. 3. a: K-feldspar; b: quartz; c: hyalophane; d: pyrite; e: MoSC phase in the Ni-Mo polymetallic ore; f: sphalerite (ZnS); g: chalcopyrite ($CuFeS_2$); h: carbonate fluorapatite.

nodules. Similarly, the major elements in the TX-1 well are also dominated by SiO_2 (average 59.6%), Al_2O_3 (average 12.3%) and Fe_2O_3 (average 5.6%), but the P_2O_5 content in the basal shales is as high as 3.7%, far higher than the value of 0.3% observed for the GMD-1 well samples.

4.2.2. Trace elements

The concentrations of selected trace elements are listed in Table 2. As illustrated in Figs. 6 and 7, a close correlation was observed between trace elements and TOC. The upper unit of the GMD-1 well has significantly lower concentrations of Ba_{XS} (avg. 8042 ppm), V (avg. 363 ppm), Ni (avg. 79 ppm) and the enrichment factors of Mo (avg. 27) and U (avg. 8) than the lower unit whose respective average concentrations of Ba_{XS}, V, and Ni are 20,480 ppm, 1734 ppm and 181 ppm with average Mo and U enrichment factors of 130 and 38, respectively (Figs. 6 and 7). It is worth noting that the lower and middle units are characterized by abnormally high concentrations of Ba_{XS}, ranging from 4266 to 76,679 ppm. The concentration of Ni and the Mo enrichment factors of the middle unit have maximum values of 387 ppm and 418, respectively, which are 3–6 times higher than those of the upper unit.

For the TX-1 well, the variation trend of trace element content is similar to that for the GMD-1 well, and the upper unit displays notably lower concentrations of Ba_{XS} (avg. 1590 ppm), V (avg. 323 ppm), Ni (avg. 86 ppm) than those of the lower unit. Two samples from the middle unit display extremely high enrichment factors of Mo (avg. 702) and U (avg. 105). Compared to the GMD-1 well, the TX-1 well has obviously low Ba_{XS} concentrations (Figs. 6 and 7).

4.2.3. Rare earth elements

Concentrations of rare earth elements (REEs) and selected ratios are listed in Table 3. The total concentrations of rare earth elements (ΣREEs) of samples from the GMD-1 well range from 139 to 343 ppm with a median value of 203 ppm, greater than the 185 ppm of the PAAS standard; samples from the TX-1 well have ΣREE values in the range of 154–686 ppm with an average of 254 ppm.

PAAS-normalized REEs reveals different distribution patterns

Table 1
Concentrations of major oxides for studied samples.

Sample	Depth	Lithology	SiO_2 (%)	Al_2O_3 (%)	TFe_2O_3 (%)	CaO (%)	MgO (%)	K_2O (%)	Na_2O (%)	TiO_2 (%)	P_2O_5 (%)	MnO (%)
GMD-1	1587.0	Gray silty shale	59.57	16.50	5.95	0.98	2.66	2.95	1.88	0.66	0.16	0.05
GMD-2	1590.0	Gray silty shale	61.93	16.23	5.86	0.95	2.69	2.98	2.05	0.71	0.16	0.05
GMD-3	1592.8	Gray silty shale	63.76	13.74	6.22	1.95	2.71	2.01	2.20	0.65	0.19	0.09
GMD-4	1599.3	Gray silty shale	60.18	15.80	5.52	1.73	2.74	2.58	2.53	0.69	0.16	0.07
GMD-5	1603.4	Gray silty shale	59.81	14.29	5.79	2.12	1.86	2.54	2.46	0.66	0.20	0.06
GMD-6	1607.2	Gray silty shale	60.63	15.61	3.23	2.04	2.16	2.76	2.75	0.58	0.12	0.06
GMD-7	1611.3	Gray silty shale	59.75	12.94	4.55	2.34	2.10	1.99	3.31	0.52	0.17	0.04
GMD-8	1614.2	Carbonaceous shale	55.80	13.47	4.47	3.86	2.78	2.04	3.36	0.50	0.13	0.06
GMD-9	1616.1	Carbonaceous shale	53.60	14.38	6.83	2.70	2.30	2.21	3.10	0.50	0.13	0.05
GMD-10	1618.1	Carbonaceous shale	53.38	12.89	4.25	5.02	3.21	2.07	2.84	0.49	0.16	0.07
GMD-11	1622.4	Carbonaceous shale	53.78	13.08	4.69	3.06	1.94	1.92	2.16	0.47	0.12	0.01
GMD-12	1625.0	Carbonaceous shale	55.15	10.87	4.13	4.77	1.28	1.78	1.58	0.41	0.18	0.01
GMD-13	1628.2	Carbonaceous shale	59.85	9.29	2.96	2.21	1.52	1.64	0.52	0.37	0.15	-
GMD-14	1630.7	Carbonaceous shale	62.44	6.92	3.40	3.46	0.71	1.34	0.04	0.30	0.19	-
GMD-15	1632.9	Carbonaceous shale	64.89	10.30	3.90	0.56	0.42	2.10	1.24	0.51	0.17	-
GMD-16	1635.1	Carbonaceous shale	58.80	10.24	4.13	0.34	0.71	2.34	0.59	0.51	0.17	-
GMD-17	1638.3	Carbonaceous shale	65.59	9.22	3.81	0.53	0.48	2.00	0.86	0.46	0.15	-
GMD-18	1641.6	Carbonaceous shale	65.15	10.14	4.02	0.60	0.45	2.02	1.23	0.48	0.17	-
GMD-19	1643.9	Carbonaceous shale	64.30	10.26	4.11	0.69	0.33	2.14	1.62	0.52	0.16	-
GMD-20	1647.9	Carbonaceous shale	63.59	11.33	3.93	0.95	0.58	2.55	1.90	0.60	0.17	-
GMD-21	1653.1	Carbonaceous shale	62.56	11.14	4.69	0.95	0.60	2.45	1.74	0.58	0.16	-
GMD-22	1655.8	Carbonaceous shale	65.72	9.53	3.45	0.79	0.88	2.03	1.31	0.52	0.16	-
GMD-23	1659.2	Carbonaceous shale	56.68	12.21	3.89	0.51	1.45	2.18	1.50	0.67	0.22	-
GMD-24	1663.1	Carbonaceous shale	62.60	11.60	4.19	0.53	0.35	2.06	2.42	0.60	0.17	-
GMD-25	1665.1	Carbonaceous shale	62.34	11.32	5.16	0.72	0.58	2.17	2.51	0.58	0.16	-
GMD-26	1668.1	Carbonaceous shale	63.32	10.94	5.46	1.36	1.64	2.10	2.37	0.54	0.14	0.02
GMD-27	1670.8	Carbonaceous shale	66.36	11.62	3.59	1.02	0.83	2.46	2.45	0.61	0.22	0.01
GMD-28	1673.1	Carbonaceous shale	66.29	10.84	2.92	0.68	0.65	2.28	2.51	0.57	0.16	0.00
GMD-29	1676.8	Carbonaceous shale	62.04	5.82	2.26	8.88	1.35	1.01	1.07	0.29	0.11	0.06
GMD-30	1677.9	Carbonaceous shale	68.91	9.43	2.83	1.95	0.70	1.90	1.92	0.50	0.18	0.02
GMD-31	1680.7	Carbonaceous shale	67.45	9.82	3.19	2.43	0.90	1.85	2.03	0.50	0.22	0.02
GMD-32	1683.0	Carbonaceous shale	60.97	7.11	3.82	6.06	2.35	1.07	1.59	0.35	0.16	0.05
GMD-33	1685.4	Carbonaceous shale	66.08	9.01	4.43	1.81	0.53	1.94	2.00	0.46	0.14	0.02
GMD-34	1689.7	Carbonaceous shale	63.70	8.98	6.33	2.29	0.59	2.04	2.10	0.46	0.17	0.03
GMD-35	1690.5	Carbonaceous shale	68.82	10.00	3.11	1.00	1.05	2.20	2.02	0.50	0.19	0.02
GMD-36	1692.9	Carbonaceous shale	67.94	9.24	3.92	1.91	0.66	2.06	2.14	0.48	0.21	0.02
GMD-37	1693.5	Carbonaceous shale	68.30	9.80	3.60	1.54	0.98	2.14	1.82	0.51	0.20	0.02
GMD-38	1695.0	Carbonaceous shale	68.19	9.67	4.36	1.64	0.64	2.13	2.12	0.50	0.19	0.02
GMD-39	1696.4	Carbonaceous shale	71.49	7.94	3.15	1.91	0.83	1.62	1.38	0.40	0.16	0.03
GMD-40	1698.9	Carbonaceous shale	65.98	6.10	2.77	4.43	5.59	0.85	0.81	0.28	0.30	0.06
GMD-41	1701.9	Cherty shale	67.44	8.32	3.96	2.22	2.17	1.64	1.57	0.40	0.17	0.03
GMD-42	1702.1	Cherty shale	67.64	8.67	3.71	1.77	1.00	1.94	1.65	0.45	0.15	0.02
GMD-43	1704.1	Cherty shale	69.49	8.16	3.25	1.88	0.74	1.63	1.54	0.39	0.15	0.02
GMD-44	1707.0	Phosphorous shale	75.22	5.19	2.90	1.80	0.68	1.09	0.48	0.22	0.29	0.01
TX-1	1751.1	Gray silty shale	56.70	20.08	6.73	0.22	2.43	4.58	1.04	0.83	0.09	0.05
TX-2	1754.2	Gray silty shale	60.02	14.83	5.63	1.05	2.27	3.40	1.21	0.60	0.09	0.05
TX-3	1758.6	Gray silty shale	59.21	17.13	7.29	0.35	2.87	4.01	1.54	0.63	0.05	0.04
TX-4	1762.1	Gray silty shale	59.55	18.00	6.86	0.29	2.22	3.89	1.08	0.83	0.07	0.05
TX-5	1766.2	Gray silty shale	65.66	13.79	5.29	1.01	2.15	3.15	1.27	0.58	0.07	0.05
TX-6	1769.1	Gray silty shale	49.93	22.80	7.47	0.25	2.88	5.87	0.94	1.00	0.11	0.04
TX-7	1772.2	Gray silty shale	57.39	18.55	6.33	0.43	2.65	4.45	1.32	0.78	0.11	0.04
TX-8	1775.6	Carbonaceous shale	62.94	11.33	3.96	1.58	1.58	2.51	1.01	0.45	0.14	0.04
TX-9	1779.1	Carbonaceous shale	57.77	11.11	6.14	1.99	1.58	2.51	1.43	0.47	0.21	0.05
TX-10	1783.2	Carbonaceous shale	60.60	8.93	5.54	2.04	1.20	1.95	1.46	0.38	0.14	0.05
TX-11	1788.6	Carbonaceous shale	69.66	6.27	3.17	2.37	0.83	1.41	0.89	0.27	0.27	0.05
TX-12	1791.1	Carbonaceous shale	63.99	6.50	4.27	3.60	0.95	1.45	1.04	0.30	0.32	0.05
TX-13	1797.3	Carbonaceous shale	72.02	5.35	3.16	2.14	0.57	1.19	0.89	0.27	0.18	0.05
TX-14	1800.1	Carbonaceous shale	58.99	11.13	5.80	1.19	0.88	2.41	1.99	0.65	0.32	0.04
TX-15	1804.8	Carbonaceous shale	56.91	10.39	4.00	4.06	1.40	2.41	1.55	0.55	1.72	0.04
TX-16	1813.7	Carbonaceous shale	50.64	6.18	5.66	5.28	0.92	1.43	0.89	0.38	0.11	0.04
TX-17	1817.1	Phosphatic shale	51.71	6.20	7.13	6.44	1.70	1.45	0.62	0.27	3.71	0.06

-, the concentration of major element oxides is < 0.0015%.

between samples of the two wells. Samples of the GMD-1 well display a convex pattern with strongly positive Eu anomalies (1.7–15.9) and slightly negative Ce anomalies (0.3–0.8) (Fig. 8a, c, and e), which is similar to the Dahebian section, where positive Eu anomalies (3.2–8.4) (Fig. 8g and h) are also present; however, samples of the TX-1 well exhibit a relatively flat pattern with slightly negative Ce anomalies (0.4–1.0) and slightly positive Eu anomalies (0.9–1.5) (Fig. 8b, d, and f).

5. Discussion

5.1. Primary productivity

A variety of geochemical proxies have been used to investigate the changes in primary productivity, including carbon and nitrogen stable isotopes, molecular biomarkers, total organic carbon content and the abundances of selected trace metals (Ba, P, Cu, Ni, and Zn) (Algeo et al., 2011; Schenau et al., 2005; Schoepfer et al., 2015; Tribovillard et al.,

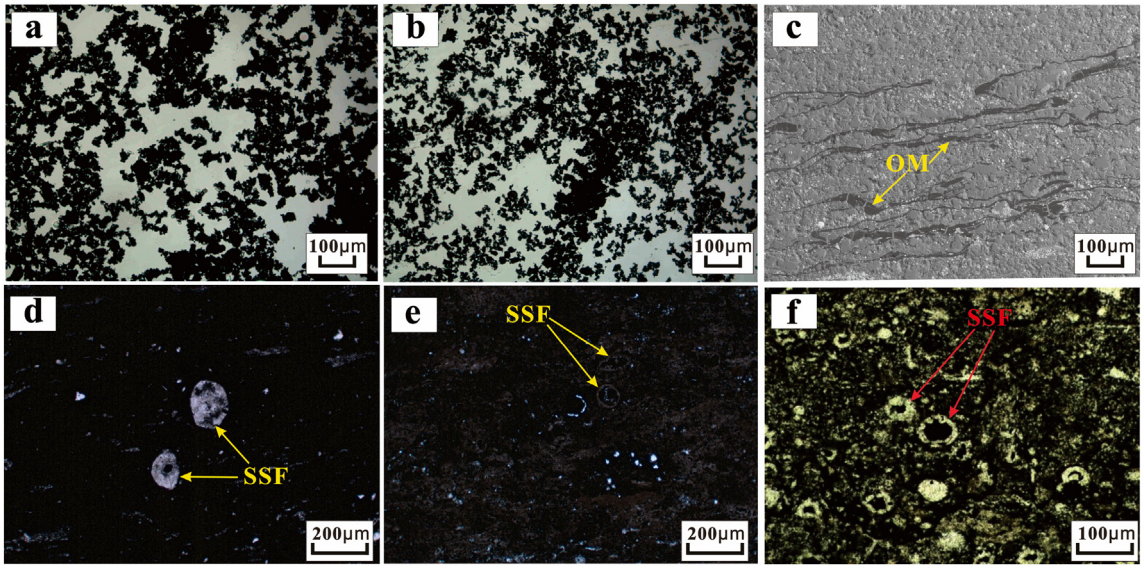

Fig. 5. Photomicrographs showing OM and bio-fossils in the Niutitang Formation shales. SSF = small shelly fossils. a: Kerogen macerals of GMD-1 well (1655.77 m); b: kerogen macerals of TX-1well (1800.12 m); c: SEM image showing stripped organic matter (GMD-1, 1690.53 m); d: SSF filled with silica in the lower unit of GMD-1 well (1632.87 m); e: SSF in the lower unit of GMD-1 well (1648.18 m); f: SSF in the lower unit of TX-1 well (1788.57 m).

2006; Tyrrell, 1999; Wei et al., 2012). In this study, the primary productivity will be estimated according to the TOC and Ba_{XS} as well as the contents of nutrient elements such as P, Cu and Ni.

Excess Ba concentrations are commonly elevated (~1000–5000 ppm) in high productivity regions of the modern equatorial Pacific (Murray and Leinen, 1993). For the GMD-1 well in the shelf region, most samples of the upper unit exhibit moderate values of Ba_{xs} (avg. 8042 ppm), whereas samples from the lower and middle units have much higher Ba_{xs} concentrations ranging from 4267 to 76,679 ppm with an average of 21,984 ppm (Fig. 6). For the TX-1 well in the slope region, Ba_{xs} concentrations in the upper unit range from 109 to 5301 ppm with an average of 1590 ppm, whereas their average value is as high as 6663 ppm in the lower unit (Fig. 7). Based on Ba_{xs} concentrations, the lower unit has a higher marine productivity than the upper unit.

Some authors argued that some Ba_{xs} may originate from hydrothermal sources (Han et al., 2015; Liu et al., 2007; Xia et al., 2005; Yang et al., 2008), therefore, the Ba_{xs} alone cannot reflect the true primary marine productivity and the relationship between TOC and Ba_{xs} has to be examined for the validity of Ba_{xs} as indicator of marine productivity (McManus et al., 1999; Schoepfer et al., 2015; Gao et al., 2016; Zhang et al., 2016). In this study, there is a good positive correlation between TOC and Ba_{xs} concentrations ($r = 0.8$, $P(\alpha) < 0.01$, $n = 17$) for samples from the TX-1 well, indicating that both proxies can be used to estimate marine productivity (Fig. 9). For samples from the GMD-1 well, a moderate correlation between TOC and Ba_{xs} was observed with a correlation coefficient of $r = 0.47$, $P(\alpha) < 0.01$, $n = 44$ (Fig. 9), and such a low correlation is probably influenced by the Ba-rich hydrothermal inputs. Although more studies are needed to identify the sharp increase in Ba_{xs} concentration, the high Ba_{xs} concentration can still be used to indicate elevated productivity in surface waters during the early Cambrian (Li et al., 2018; Zhang et al., 2016).

Some nutrient elements, including P, Cu and Ni, are also considered productivity proxies (Schenau et al., 2005; Schoepfer et al., 2015; Tribovillard et al., 2006; Tyrrell, 1999; Wei et al., 2012). As illustrated in Fig. 6, samples of the GMD-1 well have greater P/Al and Ni/Al ratios than the PAAS/Al baselines, indicating high primary productivity; in particular, these ratios in the upper unit are lower than those in the lower and middle units (Fig. 6), reflecting a decreasing primary productivity with time. A similar trend of the P/Al and Ni/Al ratios is also observed in the TX-1 well in the slope region (Fig. 7). In summary, the marine productivity was higher during the deposition of the lower and middle units than that during the deposition of the upper unit.

5.2. Evolution of redox conditions

Many redox geochemical proxies, including sensitive trace element concentrations and their ratios, the Mo-U relationship, and Fe speciation, have been widely used as indicators of redox conditions (Algeo and Maynard, 2004; Algeo and Tribovillard, 2009; Canfield et al., 2008; Hatch and Leventhal, 1992; Rimmer, 2004; Tribovillard et al., 2012). It is also necessary to study the hydrographic conditions to determine whether the early Cambrian ocean in South China is well connected with the open ocean before discussing local redox conditions. The crossplot of Mo-TOC has been proposed as an indicator of water restriction, and it primarily depends on the fact that the Mo concentration in sediments is related to the aqueous concentration of Mo and OM abundance (Algeo and Lyons, 2006; Algeo and Rowe, 2012). As illustrated in Fig. 10, the Mo/TOC ratios of the TX-1 well and Dahebian section in the slope to basinal regions fall between those of modern Cariaco and Framvaren basins, indicating weakly to moderately restricted water conditions; however, samples from the GMD-1 well in the shelf exhibit lower Mo/TOC ratios that are close to those of modern Framvaren basins (Fig. 10), indicating moderately restricted water conditions. Based on the stratigraphic correlations, redox conditions for the different units from the shallow shelf to the deep water slope during the early Cambrian on the Yangtze carbonate platform are discussed and explored below with redox geochemical proxies.

5.2.1. Deposition of the lower unit: widespread anoxic/euxinic conditions

Some trace elements (Mo, U, V) are redox sensitive and become moderately to highly enriched under anoxic bottom water conditions (Algeo and Maynard, 2004; Algeo and Rowe, 2012; Tribovillard et al., 2006). U/Th ratios of > 1.25, 0.75–1.25 and < 0.75 indicate suboxic-anoxic, dysoxic and oxic waters, respectively (Jones and Manning, 1994). Patterns of Mo_{EF}-U_{EF} covariations are also used to identify various redox conditions and particulate shuttles of marine systems based on the study of three different modern marine environments (Algeo and Tribovillard, 2009; Tribovillard et al., 2012). In this study, samples from the lower unit of the GMD-1 well in the shallow shelf show high concentrations of V (avg. 1734 ppm), Mo (avg. 62 ppm), and U (avg. 55 ppm), indicating possible anoxic bottom waters. The trace element

Table 2
Trace elemental data and main element ratios for studied samples.

Sample	Depth (m)	Lithology	TOC (wt%)	Ba_{XS}	U	Mo	V	Ni	Sc	Cr/Al $\times10^{-4}$	Zn/Al $\times10^{-4}$	Cu/Al $\times10^{-4}$	Ni/Al $\times10^{-4}$	P/Al $\times10^{-4}$	U/Th	Mo_{EF}	U_{EF}
				ppm													
GMD-1	1587.0	Gray silty shale	1.83	2492.21	14.40	21.40	464.00	77.00	18.60	12.13	15.11	7.21	8.81	79.97	1.16	24.50	5.32
GMD-2	1590.0	Gray silty shale	1.90	3081.50	15.40	22.30	544.00	100.00	21.20	14.66	5.88	12.22	11.64	81.30	1.05	25.95	5.78
GMD-3	1592.8	Gray silty shale	0.66	2047.18	4.55	1.82	181.00	47.30	15.80	10.19	5.95	9.50	6.50	114.05	0.43	2.50	2.02
GMD-4	1599.3	Gray silty shale	2.10	2446.29	15.80	19.00	586.00	76.30	18.50	12.31	16.74	15.78	9.12	83.52	1.30	22.71	6.09
GMD-5	1603.4	Gray silty shale	2.14	3858.26	7.44	3.52	170.00	34.80	17.10	11.37	21.68	5.86	4.60	115.43	0.70	4.65	3.17
GMD-6	1607.2	Gray silty shale	2.42	4372.83	18.20	26.50	398.00	99.50	16.40	12.83	1.28	8.91	12.04	63.40	1.42	32.07	7.10
GMD-7	1611.3	Gray silty shale	2.60	4234.71	35.10	36.20	529.00	128.00	16.40	13.09	10.96	13.71	18.68	108.35	3.38	52.84	16.53
GMD-8	1614.2	Carbonaceous shale	3.24	6716.47	18.80	19.20	276.00	87.30	17.10	12.75	5.02	14.72	12.24	79.59	1.79	26.92	8.50
GMD-9	1616.1	Carbonaceous shale	3.34	11,205.16	14.00	15.70	188.00	66.80	15.30	13.27	3.15	12.56	8.77	74.56	1.47	20.62	5.93
GMD-10	1618.1	Carbonaceous shale	2.65	10,856.43	19.20	18.10	399.00	86.50	15.60	11.24	10.04	16.71	12.68	102.37	2.04	26.52	9.08
GMD-11	1622.4	Carbonaceous shale	3.74	37,149.89	36.00	40.00	258.00	65.80	15.50	12.10	19.06	14.87	9.50	75.66	3.68	57.76	16.77
GMD-12	1625.0	Carbonaceous shale	5.15	30,825.94	60.70	89.90	1550.00	244.00	13.70	16.25	29.89	20.85	42.40	136.57	6.10	156.22	34.03
GMD-13	1628.2	Carbonaceous shale	6.46	35,680.31	54.20	133.00	4570.00	370.00	11.60	32.74	209.42	40.87	75.23	133.16	6.22	270.42	35.55
GMD-14	1630.7	Carbonaceous shale	6.97	44,561.87	134.00	153.00	2000.00	387.00	7.35	26.07	105.91	53.23	105.64	226.44	17.77	417.63	117.99
GMD-15	1632.9	Carbonaceous shale	8.74	40,845.56	56.60	60.80	946.00	152.00	11.70	15.99	55.02	10.14	27.87	136.12	5.80	111.50	33.48
GMD-16	1635.1	Carbonaceous shale	10.68	28,847.62	84.10	75.80	315.00	167.00	11.90	14.02	14.13	15.53	30.81	136.92	7.58	139.82	50.04
GMD-17	1638.3	Carbonaceous shale	6.19	50,082.72	52.90	45.90	535.00	89.80	9.61	15.98	30.94	15.04	18.40	134.17	5.57	94.03	34.96
GMD-18	1641.6	Carbonaceous shale	5.23	32,051.06	53.40	49.10	935.00	119.00	9.34	14.06	31.30	15.63	22.17	138.27	5.86	91.46	32.09
GMD-19	1643.9	Carbonaceous shale	5.67	44,346.94	72.30	55.80	181.00	133.00	9.24	15.70	5.54	15.11	24.49	128.61	7.23	102.73	42.94
GMD-20	1647.9	Carbonaceous shale	5.62	38,310.11	49.60	62.60	1090.00	179.00	8.06	13.30	5.87	20.01	29.84	123.75	4.59	104.36	26.67
GMD-21	1653.1	Carbonaceous shale	5.51	38,016.65	81.20	83.00	434.00	180.00	12.60	12.99	23.91	7.97	30.52	118.45	7.38	140.73	44.41
GMD-22	1655.8	Carbonaceous shale	5.41	35,272.06	59.50	100.00	2840.00	315.00	13.90	23.39	60.25	16.29	62.43	138.46	5.61	198.20	38.04
GMD-23	1659.2	Carbonaceous shale	6.29	76,679.83	86.70	107.00	1270.00	360.00	16.50	17.64	29.55	14.97	55.69	148.60	6.19	165.53	43.27
GMD-24	1663.1	Carbonaceous shale	7.31	38,800.82	52.00	53.20	230.00	189.00	16.50	14.83	4.49	12.26	30.78	120.87	3.77	86.63	27.31
GMD-25	1665.1	Carbonaceous shale	5.60	20,210.46	47.60	42.20	224.00	72.00	13.00	13.22	13.97	12.20	12.01	116.57	4.41	70.42	25.62
GMD-26	1668.1	Carbonaceous shale	5.70	23,723.54	46.30	32.80	364.00	116.00	15.70	13.00	9.22	19.34	20.03	105.54	4.13	56.63	25.79
GMD-27	1670.8	Carbonaceous shale	5.25	16,700.14	66.00	77.50	2930.00	188.00	14.20	20.81	17.56	13.72	30.56	156.14	5.16	125.98	34.61
GMD-28	1673.1	Carbonaceous shale	4.19	17,326.98	49.30	41.40	1800.00	157.00	10.40	17.60	75.80	19.17	27.36	121.73	4.21	72.14	27.71
GMD-29	1676.8	Carbonaceous shale	3.96	8729.72	70.70	80.10	630.00	209.00	8.33	17.95	8.47	17.85	67.83	155.88	11.80	259.97	74.02
GMD-30	1677.9	Carbonaceous shale	4.61	10,175.50	28.10	61.90	2730.00	206.00	8.01	25.24	17.37	20.23	41.26	157.42	2.86	123.99	18.16
GMD-31	1680.7	Carbonaceous shale	5.11	6782.08	32.60	59.40	3660.00	242.00	11.40	43.09	181.39	13.96	46.55	184.77	3.97	114.26	20.23
GMD-32	1683.0	Carbonaceous shale	6.60	6685.33	56.30	62.30	275.00	185.00	9.72	1.38	39.32	13.04	49.15	185.59	9.23	165.51	48.25
GMD-33	1685.4	Carbonaceous shale	6.32	7719.95	27.60	34.20	800.00	131.00	10.10	12.89	58.49	13.63	27.46	128.15	3.91	71.70	18.67
GMD-34	1689.7	Carbonaceous shale	5.82	8840.98	48.20	68.00	769.00	168.00	9.40	9.36	6.33	10.16	35.34	156.13	6.13	143.03	32.71
GMD-35	1690.5	Carbonaceous shale	7.20	7485.88	50.90	45.30	2500.00	113.00	11.70	17.45	68.94	8.84	21.34	156.70	5.34	85.57	31.01
GMD-36	1692.9	Carbonaceous shale	7.57	6552.04	34.00	63.80	1480.00	179.00	7.06	26.17	59.28	10.92	36.59	187.44	4.57	130.42	22.42
GMD-37	1693.5	Carbonaceous shale	6.69	6062.76	32.40	41.30	3420.00	207.00	10.30	89.43	553.17	33.73	39.90	168.31	3.84	79.60	20.14
GMD-38	1695.0	Carbonaceous shale	5.36	7447.24	30.20	57.40	2000.00	207.00	9.55	29.30	42.97	11.45	40.43	162.05	3.56	112.12	19.03
GMD-39	1696.4	Carbonaceous shale	5.53	4266.77	25.30	63.40	4320.00	247.00	8.80	100.39	604.25	41.87	58.76	166.19	3.80	150.83	19.42
GMD-40	1698.9	Carbonaceous shale	4.74	7060.09	164.00	65.50	948.00	79.50	7.52	1.95	51.40	35.92	24.62	405.60	30.71	202.82	163.82
GMD-41	1701.9	Cherty shale	4.84	6803.69	37.60	44.60	1180.00	119.00	9.36	19.77	32.24	13.39	27.02	168.51	5.27	101.26	27.54
GMD-42	1702.1	Cherty shale	4.86	6371.65	30.40	46.30	2430.00	163.00	9.09	33.33	488.02	28.54	35.51	142.69	4.10	100.87	21.36
GMD-43	1704.1	Cherty shale	5.04	5999.20	51.80	131.00	3920.00	289.00	8.90	72.69	861.11	68.06	66.90	151.60	7.80	303.24	38.68
GMD-44	1707.0	Phosphorous shale	4.86	6211.40	57.60	54.60	6870.00	271.00	5.82	833.44	1244.70	103.36	98.63	460.83	11.71	198.72	67.62
TX-1	1751.1	Gray silty shale	0.73	260.85	2.88	9.80	137.00	60.00	14.20	11.10	8.94	6.82	5.64	37.63	0.33	9.22	0.87
TX-2	1754.2	Gray silty shale	1.66	521.65	4.08	14.40	109.00	59.00	16.70	15.29	10.70	8.76	7.52	50.96	0.29	18.34	1.68
TX-3	1758.6	Gray silty shale	1.15	109.05	5.33	16.30	126.00	60.00	14.10	11.03	17.97	6.69	6.62	22.05	0.57	17.97	1.90
TX-4	1762.1	Gray silty shale	1.43	202.15	6.80	20.60	112.00	54.00	15.10	8.92	10.49	7.01	5.67	31.48	0.64	21.62	2.30
TX-5	1766.2	Gray silty shale	1.13	465.90	5.28	21.90	155.00	72.00	14.80	12.74	11.23	9.23	9.86	41.10	0.53	30.00	2.33
TX-6	1769.1	Gray silty shale	1.47	318.95	5.68	21.10	195.00	69.00	15.10	12.34	5.05	5.80	5.72	41.43	0.55	17.48	1.52
TX-7	1772.2	Gray silty shale	1.27	481.00	5.96	20.90	343.00	87.00	14.10	13.75	8.45	8.04	8.86	50.92	0.60	21.28	1.96
TX-8	1775.6	Carbonaceous shale	4.14	3395.00	19.47	84.40	1273.00	162.00	16.00	46.67	138.67	44.20	27.00	100.00	2.26	140.67	10.47

(*continued on next page*)

Table 2 (*continued*)

Sample	Depth (m)	Lithology	TOC (wt%)	Ba_{XS}	U	Mo	V	Ni	Sc	Cr/Al	Zn/Al	Cu/Al	Ni/Al	P/Al	U/Th	Mo_{EF}	U_{EF}
				ppm						$\times 10^{-4}$	$\times 10^{-4}$	$\times 10^{-4}$	$\times 10^{-4}$	$\times 10^{-4}$			
TX-9	1779.1	Carbonaceous shale	5.11	4843.80	33.00	82.80	599.00	144.00	19.40	45.41	26.02	24.42	24.49	153.06	3.00	140.82	18.10
TX-10	1783.2	Carbonaceous shale	5.80	5300.65	48.18	89.40	184.00	90.00	17.90	71.25	27.70	28.20	19.03	126.85	4.77	189.01	32.86
TX-11	1788.6	Carbonaceous shale	5.10	4856.60	48.73	147.50	1547.00	216.00	13.10	168.07	130.42	50.69	65.06	361.45	6.09	444.28	47.35
TX-12	1791.1	Carbonaceous shale	6.77	7768.30	173.80	330.10	662.00	367.00	13.20	51.74	82.27	28.90	106.69	406.98	18.10	959.59	162.98
TX-13	1797.3	Carbonaceous shale	6.02	6133.85	83.49	112.60	108.00	85.00	11.00	150.18	40.64	30.28	30.04	282.69	12.10	397.88	95.17
TX-14	1800.1	Carbonaceous shale	6.04	5091.15	57.86	79.60	622.00	238.00	13.90	67.23	36.50	14.45	40.41	237.69	5.51	135.14	31.69
TX-15	1804.8	Carbonaceous shale	5.49	4235.70	26.84	67.50	3321.00	196.00	18.30	148.36	685.09	89.95	35.64	1363.64	2.24	122.73	15.74
TX-16	1813.7	Carbonaceous shale	5.51	14,318.45	26.73	73.00	1410.00	128.00	21.30	113.76	58.72	19.30	39.14	152.91	4.38	223.24	26.37
TX-17	1817.1	Phosphatic shale	5.05	4238.40	71.06	93.50	7496.00	218.00	13.00	896.34	1964.02	150.30	66.46	4939.02	10.01	285.06	69.89

ratios of U/Th (avg. 6.5) also indicate anoxic water conditions (Fig. 6). This inference is consistent with the high and variable enrichment factors of Mo and U, and the Mo_{EF}/U_{EF} ratios are 1–3 times that of seawater, indicating predominant anoxic conditions with intermittent redox changes from anoxic to euxinic (Fig. 11). Similar high concentrations of sensitive trace elements and U/Th ratios are also observed in samples from the lower unit of the TX-1 well in the deep water slope region (Fig. 7) and the contemporaneous black shales of the Dahebian section in the basinal region (Han et al., 2015), suggesting the extensive presence of anoxic water from the shallow shelf to the deep water slope and basinal regions. Early studies also argued for the widespread anoxic and ferruginous water conditions from the shallow shelf to slope regions on the Yangtze Platform based on Fe speciation data during Cambrian Stage 2 and 3 (Jin et al., 2016; Wang et al., 2012; Y. Zhang et al., 2017). It is worth noting that temporarily sulfidic water conditions may exist during the deposition of the widespread polymetallic Ni-Mo sulfidic layer at the base of the lower unit (S.Y. Jiang et al., 2007a; Lehmann et al., 2007; Wille et al., 2008; Xu et al., 2013). All these facts indicate that dominant anoxic/euxinic with intermittent sulfide water conditions prevailed from the shallow shelf to deep water slope and basinal regions during Stage 2 and early Stage 3.

5.2.2. Deposition of the middle unit: diminishing anoxic water conditions

Compared with the lower unit, the middle units of both the GMD-1 well and TX-1 well show obviously high concentrations of Mo (avg. 125 ppm and 239 ppm, respectively) and U (avg. 83 ppm and 111 ppm, respectively), indicating more reducing water conditions. For the GMD-1 well in the shallow shelf, the relatively high trace element ratios of U/Th (avg. 10) suggest anoxic water conditions (Fig. 6). These parameters from the middle unit of TX-1 in the slope setting also reflect similar anoxic water conditions. These results are also supported by the diagram of U_{EF}-Mo_{EF} (Fig. 11) and most samples from the middle units of the GMD-1 well and the TX-1 well are plotted in the region of anoxic to euxinic conditions. It is worthy to note that the middle unit samples of the GMD-1 and TX-1 wells show higher enrichment factors of Mo (avg. 151 and 702, respectively) and U (avg. 56 and 105, respectively) (Figs. 6 and 7) than the samples of the lower units. Algeo and Maynard (2004) investigated the contrasting behavior of trace elements under different sedimentary environments and proposed that relatively high concurrent enrichments of U, V and Mo could reflect euxinic water conditions. The evident increase of Mo and U concentrations in the middle units of the two wells may indicate the transition from persistent anoxic to euxinic water conditions during their deposition. However, early studies suggested a stepwise oxygenation of the ocean during Stage 3 based on the iron speciation data (Wang et al., 2012; Li et al., 2017), and therefore higher enrichment factors of Mo and U in the middle units may be related to the relative enrichment of Mo and U in local diminishing anoxic waters while there was an expansion of oxic waters in the shelf and slope regions.

5.2.3. Deposition of the upper unit: widespread oxic water conditions

Along with expanding oxic water of the early Cambrian ocean, the low concentrations of V (avg. 363 ppm), Mo (avg. 20 ppm) and U (avg. 18 ppm) from the upper unit of the GMD-1 well in the shallow shelf suggest oxic/suboxic water conditions. Low concentrations of these redox-sensitive elements are also observed in the upper unit of the TX-1 well in the deep water slope region, reflecting possible large-scale oxic water conditions during late Stage 3. This inference is also supported by the low ratios of U/Th from the middle units of two wells (Figs. 6 and 7). In the diagram of U_{EF}-Mo_{EF} (Fig. 11), most of the upper unit samples of the GMD-1 well are plotted in the region of suboxic, whereas the upper unit samples of the TX-1 well shows low EFs of U (0.9–10.5, 2.9 on average) and moderate EFs of Mo (9.2–140.7, 34.6 on average), most of which fall into particulate shuttling region. This particulate shuttling may occur in oxic water with short-term anoxic episodes. This inference is also consistent with the results from age-equivalent gray

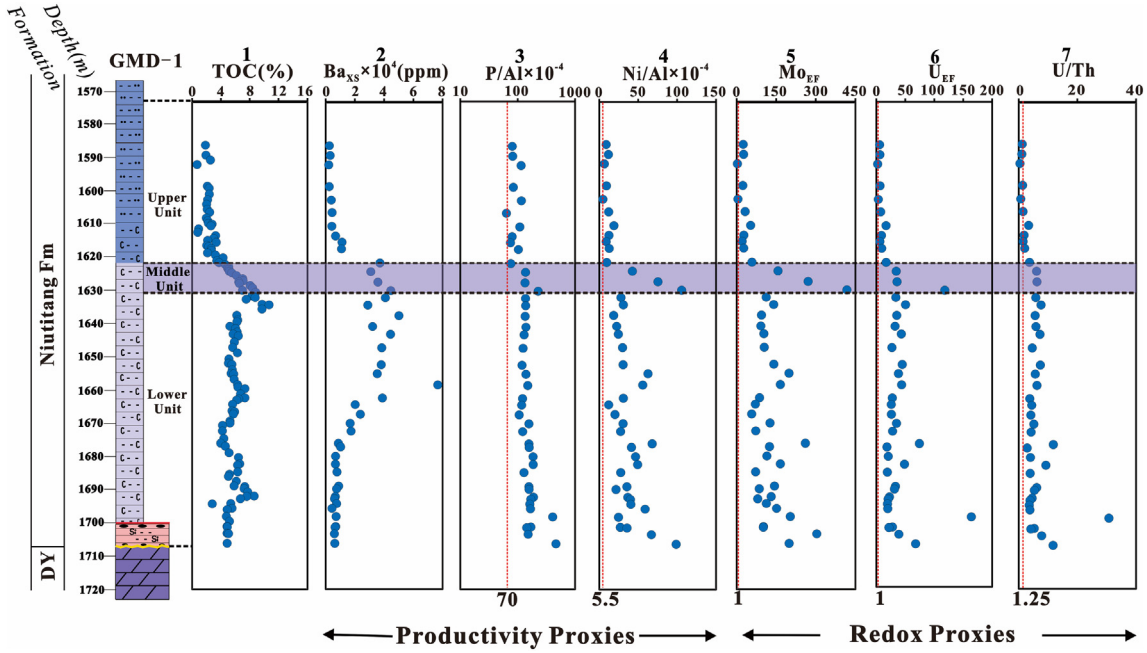

Fig. 6. Vertical variations of multiple geochemical proxies from the Niutitang Formation of GMD-1 well. Representative concentrations of P and Ni from PAAS (Taylor and McLennan, 1985) vs. Al (P/Al = 70 × 10^{-4}; Ni/Al = 5.5 × 10^{-4}) and the U/Th ratio of 1.25 tentatively used to distinguish anoxic/suboxic from dysoxic conditions (Jones and Manning, 1994) are indicated by the red vertical dashed lines. (For interpretation of the references to color in this figure legend, the reader is referred to the web version of this article.)

black shales of Shatan/Jinsha/Longbizui sections from shallow shelf to slope facies (Jin et al., 2016; K. Zhang et al., 2017; Y. Zhang et al., 2017). All these results suggest a wide expansion of oxic waters from the shallow shelf to deep water slope settings during late Stage 3.

5.3. Hydrothermal activity

Early studies proposed that the origin of the Ni-Mo polymetallic ore layer in the basal Niutitang Formation was mainly due to seafloor hydrothermal venting during Cambrian Stage 2 (Chen et al., 2006; Gao et al., 2018; Han et al., 2015; Jiang et al., 2007a; Lott et al., 1999; Steiner et al., 2001; Wang et al., 2012). In the present study area, several lines of evidence indicate that active hydrothermal activity may also occur in the shelf region during the deposition of OM-rich black shales of Cambrian Stage 3.

5.3.1. Insights from mineralogy

Previous studies have identified several minerals indicative of hydrothermal activity within Dahebian barite deposits in South China, including galena, chalcopyrite, siderite and hyalophane (Han et al., 2015; Xia et al., 2005; Yang et al., 2008). Hyalophane is a member of the feldspar group of tectosilicates and is considered to be a barium

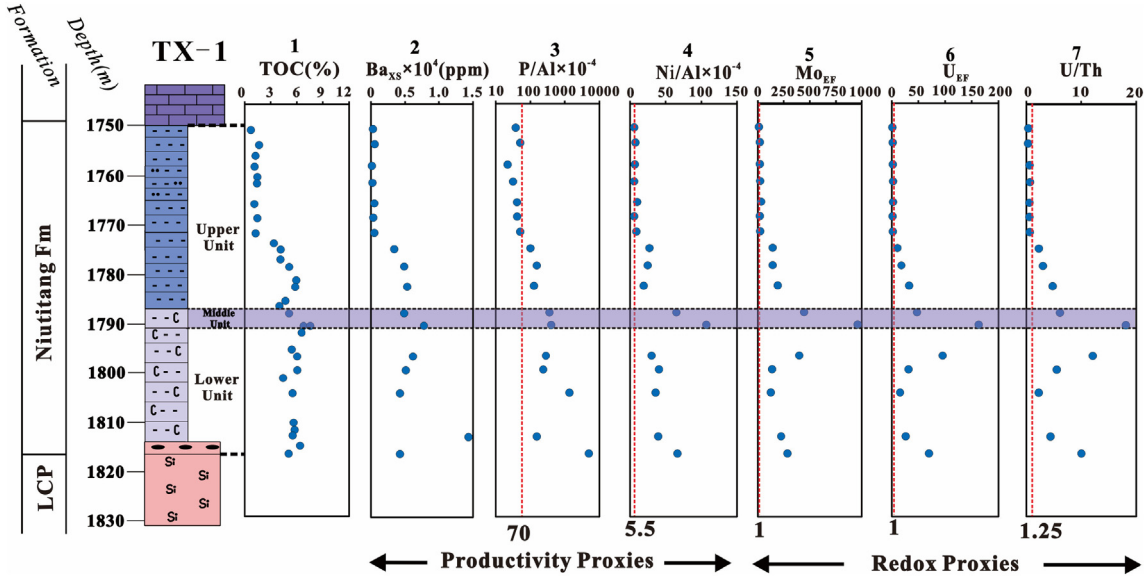

Fig. 7. Vertical variations of multiple geochemical proxies from the Niutitang Formation of TX-1 well. Representative concentrations of P and Ni from PAAS (Taylor and McLennan, 1985) vs. Al (P/Al = 70 × 10^{-4}; Ni/Al = 5.5 × 10^{-4}) and the U/Th ratio of 1.25 tentatively used to distinguish anoxic/suboxic from dysoxic conditions (Jones and Manning, 1994) are indicated by the red vertical dashed lines. (For interpretation of the references to color in this figure legend, the reader is referred to the web version of this article.)

Table 3
REE concentrations (ppm) and selected parameters for studied samples.

Sample	Depth (m)	Lithology	La	Ce	Pr	Nd	Sm	Eu	Gd	Tb	Dy	Y	Ho	Er	Tm	Yb	Lu	Total	LREE	HREE	Y/Ho	Eu/Eu*	Ce/Ce*
			ppm																				
GMD-1	1587.0	Gray silty shale	41.60	68.40	9.62	33.80	6.74	2.34	5.36	1.00	5.08	31.80	1.08	3.34	0.58	3.28	0.50	214.52	162.50	52.02	29.44	1.83	0.79
GMD-2	1590.0	Gray silty shale	50.80	80.60	11.00	37.70	7.68	2.59	6.32	1.19	5.88	35.30	1.28	3.84	0.71	3.90	0.60	249.39	190.37	59.02	27.58	1.75	0.79
GMD-3	1592.8	Gray silty shale	35.70	61.80	8.31	29.10	6.49	2.18	5.54	1.05	5.25	29.50	1.10	3.22	0.58	3.19	0.49	193.50	143.58	49.92	26.82	1.71	0.83
GMD-4	1599.3	Gray silty shale	41.00	67.00	9.22	32.10	6.57	2.14	5.56	1.05	5.35	32.80	1.15	3.47	0.64	3.50	0.54	212.09	158.03	54.06	28.52	1.67	0.80
GMD-5	1603.4	Gray silty shale	38.00	64.00	8.82	31.60	7.06	3.00	5.78	1.10	5.64	33.30	1.18	3.48	0.58	3.30	0.51	207.35	152.48	54.87	28.22	2.21	0.81
GMD-6	1607.2	Gray silty shale	43.00	70.40	9.34	30.90	5.67	2.51	4.84	0.88	4.55	27.50	1.01	3.04	0.57	3.10	0.48	207.79	161.82	45.97	27.23	2.26	0.81
GMD-7	1611.3	Gray silty shale	36.70	59.90	8.15	28.90	6.44	2.55	5.25	1.03	5.23	36.20	1.14	3.35	0.61	3.24	0.49	199.18	142.64	56.54	31.75	2.07	0.80
GMD-8	1614.2	Carbonaceous shale	34.10	56.80	7.70	26.90	6.06	3.22	5.26	1.00	4.81	31.30	1.08	3.09	0.63	3.10	0.51	185.56	134.78	50.78	28.98	2.69	0.81
GMD-9	1616.1	Carbonaceous shale	33.60	55.10	7.44	25.60	5.63	4.35	4.53	0.93	4.42	27.30	0.98	2.79	0.59	2.82	0.50	176.58	131.72	44.86	27.86	4.06	0.80
GMD-10	1618.1	Carbonaceous shale	31.90	51.30	7.03	24.70	5.66	4.44	5.00	0.90	4.44	29.60	0.98	2.84	0.58	2.81	0.47	172.65	125.03	47.62	30.20	3.93	0.79
GMD-11	1622.4	Carbonaceous shale	34.20	55.70	7.29	25.20	5.26	14.00	5.20	0.80	4.16	28.60	0.92	2.80	0.49	2.78	0.44	187.84	141.65	46.19	31.09	12.61	0.81
GMD-12	1625.0	Carbonaceous shale	39.40	60.30	8.02	27.90	6.09	10.20	6.08	1.03	5.51	44.20	1.30	3.80	0.70	3.56	0.56	218.65	151.91	66.74	34.00	7.89	0.78
GMD-13	1628.2	Carbonaceous shale	37.00	49.30	7.17	25.00	5.47	11.30	5.67	1.00	5.50	53.00	1.35	4.10	0.73	3.73	0.59	210.91	135.24	75.67	39.26	9.55	0.70
GMD-14	1630.7	Carbonaceous shale	39.30	46.90	7.14	25.70	5.48	13.60	6.07	1.04	5.84	63.00	1.47	4.48	0.79	4.02	0.62	225.45	138.12	87.33	42.86	11.10	0.64
GMD-15	1632.9	Carbonaceous shale	35.40	53.40	7.40	26.60	5.56	9.03	5.00	0.86	4.68	38.20	1.06	3.26	0.55	3.04	0.47	194.51	137.39	57.12	36.04	8.06	0.76
GMD-16	1635.1	Carbonaceous shale	39.90	62.40	7.93	26.90	5.47	9.05	4.67	0.85	4.32	32.60	0.97	2.92	0.53	2.79	0.43	201.73	151.65	50.08	33.61	8.43	0.81
GMD-17	1638.3	Carbonaceous shale	35.50	53.50	7.26	25.00	5.47	15.60	4.70	0.82	4.06	29.50	0.90	2.66	0.49	2.58	0.39	188.43	142.33	46.10	32.78	14.49	0.77
GMD-18	1641.6	Carbonaceous shale	34.50	51.90	7.03	24.50	5.35	10.20	4.80	0.87	4.49	33.90	1.02	3.01	0.54	2.79	0.43	185.33	133.48	51.85	33.24	9.48	0.77
GMD-19	1643.9	Carbonaceous shale	37.80	58.70	7.60	26.00	5.61	14.80	5.07	0.86	4.24	27.80	0.91	2.67	0.50	2.59	0.41	195.56	150.51	45.05	30.55	13.07	0.80
GMD-20	1647.9	Carbonaceous shale	38.70	60.00	7.63	25.80	5.42	12.60	4.83	0.81	3.97	24.00	0.85	2.50	0.44	2.36	0.36	190.27	150.15	40.12	28.24	11.60	0.80
GMD-21	1653.1	Carbonaceous shale	38.20	58.70	7.88	27.70	5.83	16.90	5.14	0.86	4.52	33.00	1.00	3.10	0.52	2.94	0.45	206.74	155.21	51.53	33.00	14.54	0.78
GMD-22	1655.8	Carbonaceous shale	44.50	63.50	9.13	31.60	6.69	12.80	6.06	1.10	5.68	45.80	1.29	3.86	0.69	3.57	0.54	236.81	168.22	68.59	35.50	9.47	0.73
GMD-23	1659.2	Carbonaceous shale	43.10	61.80	9.60	35.00	8.29	27.60	8.08	1.47	7.21	55.00	1.71	4.93	0.96	4.58	0.75	270.08	185.39	84.69	32.16	15.88	0.70
GMD-24	1663.1	Carbonaceous shale	49.60	74.10	10.60	37.40	8.22	14.90	7.25	1.66	7.39	45.40	2.36	5.02	1.52	4.58	1.09	271.09	194.82	76.27	19.24	9.09	0.75
GMD-25	1665.1	Carbonaceous shale	39.80	61.40	8.88	31.80	6.63	10.40	5.79	1.08	5.26	37.80	1.17	3.46	0.62	3.18	0.51	217.78	158.91	58.87	32.31	7.90	0.75
GMD-26	1668.1	Carbonaceous shale	41.20	63.10	8.90	30.70	6.55	9.45	6.15	1.25	5.88	42.00	1.40	3.86	0.80	3.67	0.63	225.54	159.90	65.64	30.00	7.01	0.76
GMD-27	1670.8	Carbonaceous shale	49.40	73.70	11.10	38.40	8.01	7.36	6.68	1.23	5.94	40.10	1.30	3.88	0.72	3.64	0.56	252.02	187.97	64.05	30.85	4.74	0.73
GMD-28	1673.1	Carbonaceous shale	42.10	63.10	9.14	31.80	6.75	7.03	5.81	1.08	5.27	34.40	1.17	3.43	0.66	3.20	0.51	215.45	159.92	55.53	29.40	5.29	0.74
GMD-29	1676.8	Carbonaceous shale	24.50	34.70	5.56	20.10	4.47	4.20	4.44	0.80	3.88	29.40	0.89	2.52	0.46	2.23	0.36	138.51	93.53	44.98	33.03	4.44	0.69
GMD-30	1677.9	Carbonaceous shale	36.40	50.90	7.47	25.80	5.11	4.55	4.38	0.75	3.40	23.00	0.75	2.20	0.43	2.14	0.36	167.64	130.23	37.41	30.67	4.53	0.71
GMD-31	1680.7	Carbonaceous shale	29.40	38.40	6.61	25.00	5.54	4.13	5.18	0.94	5.37	47.00	1.18	3.76	0.51	3.34	0.46	176.82	109.08	67.74	39.83	3.63	0.64
GMD-32	1683.0	Carbonaceous shale	29.70	40.70	6.04	21.80	4.66	3.76	4.61	0.81	4.53	42.60	1.00	3.14	0.44	2.72	0.38	166.89	106.66	60.23	42.60	3.82	0.70
GMD-33	1685.4	Carbonaceous shale	26.40	37.30	5.56	20.20	4.20	4.15	3.71	0.62	3.59	29.00	0.71	2.38	0.24	2.17	0.23	140.46	97.81	42.65	40.85	4.95	0.71
GMD-34	1689.7	Carbonaceous shale	29.70	43.90	6.55	23.70	4.91	4.79	4.20	0.69	3.91	29.40	0.78	2.58	0.28	2.35	0.26	158.00	113.55	44.45	37.69	4.97	0.73
GMD-35	1690.5	Carbonaceous shale	37.00	52.40	8.26	29.90	6.14	4.46	6.29	1.25	7.32	56.80	1.62	4.78	0.60	3.52	0.46	220.80	138.16	82.64	35.06	3.38	0.69
GMD-36	1692.9	Carbonaceous shale	27.30	38.30	6.01	22.00	4.88	3.65	4.15	0.72	4.21	33.70	0.87	2.85	0.31	2.57	0.30	151.82	102.14	49.68	38.74	3.82	0.69
GMD-37	1693.5	Carbonaceous shale	34.90	47.10	7.88	28.60	5.77	3.48	5.06	0.90	5.07	42.20	1.07	3.45	0.39	3.02	0.36	189.25	127.73	61.52	39.44	3.03	0.66
GMD-38	1695.0	Carbonaceous shale	28.50	40.00	6.32	23.30	5.22	3.92	4.67	0.84	4.96	40.60	1.06	3.42	0.39	3.00	0.36	166.56	107.26	59.30	38.30	3.74	0.69
GMD-39	1696.4	Carbonaceous shale	27.60	34.40	6.09	22.80	4.67	2.61	4.23	0.72	4.35	38.40	0.94	3.10	0.35	2.79	0.33	153.38	98.17	55.21	40.85	2.77	0.61
GMD-40	1698.9	Carbonaceous shale	56.80	69.60	12.00	45.10	9.54	4.76	9.09	1.63	8.83	85.70	2.00	5.95	0.78	4.36	0.56	316.70	197.80	118.90	42.85	2.41	0.61
GMD-41	1701.9	Cherty shale	29.30	39.00	6.57	24.60	5.08	3.96	4.92	0.84	4.76	42.80	1.15	3.56	0.58	3.12	0.50	170.74	108.51	62.23	37.22	3.73	0.65
GMD-42	1702.1	Cherty shale	27.80	36.40	6.05	21.70	4.47	3.50	3.88	0.70	3.91	32.70	0.93	2.85	0.47	2.56	0.42	148.34	99.92	48.42	35.16	3.96	0.65
GMD-43	1704.1	Cherty shale	37.50	39.40	8.05	30.00	6.25	3.59	5.96	1.21	6.57	63.00	1.76	5.11	1.06	4.29	0.84	214.59	124.79	89.80	35.80	2.77	0.52
GMD-44	1707.0	Phosphorous shale	52.70	35.70	11.20	44.80	9.65	4.42	9.71	1.97	11.00	139.00	3.11	9.04	1.81	7.25	1.34	342.70	158.47	184.23	44.69	2.15	0.34
TX-1	1751.1	Gray silty shale	31.26	55.28	7.42	27.46	3.64	1.11	4.20	0.74	4.28	22.64	0.85	2.77	0.45	3.06	0.48	165.64	126.17	39.47	26.64	1.34	0.90
TX-2	1754.2	Gray silty shale	39.64	69.13	9.64	34.95	7.12	1.20	6.07	0.84	4.82	26.31	0.93	2.76	0.42	2.66	0.40	206.89	161.68	45.21	28.29	0.86	0.87
TX-3	1758.6	Gray silty shale	28.02	48.60	6.88	26.46	3.58	1.20	4.45	0.81	4.31	22.56	0.81	2.48	0.39	2.61	0.38	153.54	114.74	38.80	27.85	1.42	0.87
TX-4	1762.1	Gray silty shale	30.52	53.88	7.26	28.42	4.28	1.37	4.73	0.81	4.42	24.95	0.81	2.54	0.41	2.73	0.40	167.53	125.73	41.80	30.80	1.43	0.89
TX-5	1766.2	Gray silty shale	31.76	55.20	7.72	29.12	4.26	1.14	4.40	0.88	4.55	24.64	0.87	2.90	0.45	3.08	0.45	171.42	129.20	42.22	28.32	1.24	0.87
TX-6	1769.1	Gray silty shale	35.28	61.68	7.65	27.44	2.81	1.00	3.60	0.77	4.65	26.03	0.99	3.31	0.56	3.81	0.59	180.17	135.86	44.31	26.29	1.48	0.92
TX-7	1772.2	Gray silty shale	32.90	58.20	7.76	29.54	3.43	1.13	3.92	0.80	4.57	24.18	0.92	3.02	0.50	3.34	0.51	174.72	132.96	41.76	26.28	1.45	0.90
TX-8	1775.6	Carbonaceous shale	35.52	64.28	8.32	32.10	6.62	1.39	7.14	0.99	6.08	41.99	1.31	4.06	0.64	4.02	0.63	215.09	148.23	66.86	32.05	0.95	0.92

(*continued on next page*)

Table 3 (*continued*)

Sample	Depth (m)	Lithology	La	Ce	Pr	Nd	Sm	Eu	Gd	Tb	Dy	Y	Ho	Er	Tm	Yb	Lu	Total	LREE	HREE	Y/Ho	Eu/Eu*	Ce/Ce*
			ppm																				
TX-9	1779.1	Carbonaceous shale	50.62	95.98	11.52	41.70	9.40	2.07	9.91	1.30	7.83	49.96	1.62	4.95	0.75	4.55	0.67	292.83	211.29	81.54	30.84	1.01	0.98
TX-10	1783.2	Carbonaceous shale	44.27	83.85	9.20	34.20	6.92	1.54	7.11	0.98	5.67	38.26	1.18	3.54	0.56	3.31	0.50	241.09	179.98	61.11	32.42	1.03	1.02
TX-11	1788.6	Carbonaceous shale	36.72	61.68	7.41	27.90	5.82	1.23	6.51	0.87	5.29	40.96	1.15	3.50	0.52	3.12	0.47	203.15	140.76	62.39	35.62	0.94	0.92
TX-12	1791.1	Carbonaceous shale	56.80	100.83	10.72	41.25	8.24	1.73	8.76	1.11	6.74	47.77	1.41	4.05	0.59	3.21	0.47	293.68	219.57	74.11	33.88	0.96	1.00
TX-13	1797.3	Carbonaceous shale	40.33	68.43	7.72	28.80	5.43	1.18	5.86	0.78	4.48	31.58	0.94	2.68	0.37	2.12	0.30	201.00	151.89	49.11	33.60	0.99	0.95
TX-14	1800.1	Carbonaceous shale	47.70	89.45	11.85	47.90	9.33	1.95	10.13	1.54	8.64	56.38	1.80	5.30	0.76	4.19	0.60	297.52	208.18	89.34	31.32	0.94	0.93
TX-15	1804.8	Carbonaceous shale	56.46	72.42	14.02	57.60	13.94	3.07	16.81	2.13	12.99	93.52	2.72	8.14	1.19	6.92	1.02	362.95	217.51	145.44	34.38	0.94	0.64
TX-16	1813.7	Carbonaceous shale	55.02	84.95	11.70	49.05	12.98	3.69	11.78	1.35	8.09	46.49	1.68	4.80	0.71	4.00	0.59	296.88	217.39	79.49	27.67	1.41	0.82
TX-17	1817.1	Phosphatic shale	104.68	89.92	24.19	106.80	24.30	5.41	31.21	3.74	24.03	236.57	5.30	15.25	2.07	11.14	1.56	686.17	355.30	330.87	44.64	0.93	0.44

feldspar commonly described from low- to medium-grade metamorphic and volcanic or magmatic systems as a substitution for feldspar minerals (Essene et al., 2005; Gao et al., 2018; Zhang et al., 1993). Hyalophane is frequently associated with Ba-rich hydrothermal fluids and thus generally regarded as evidence of hydrothermal activity (Gao et al., 2018; Han et al., 2015; Hou et al., 2001; Kribek et al., 1996). The samples showing no hyalophane from TX-1 well yield moderate correlation coefficients (r) between Ba_{XS} and typical elements of terrestrial inputs Ti, Al, Sc ($r = -0.67, -0.78, +0.38$, respectively, $n = 17$) (Fig. 12), indicating the contribution of terrestrial Ba inputs; however, the samples containing hyalophane from GMD-1 well show poor correlation coefficients (r) between Ba_{XS} and typical elements of terrestrial inputs Ti, Al, and Sc ($r = +0.07, -0.07, +0.03$, respectively, $n = 44$) (Fig. 12), ruling out significant or dominant terrestrial Ba inputs.

In addition, some authors explored the relationship between hyalophane and surrounding minerals in ore deposits and proposed that the presence of hyalophane is related to hydrothermally induced diagenetic alteration of K-feldspar (Gao et al., 2018; Kribek et al., 1996; Riegler and McClenaghan, 2017). For example, Gao et al. (2018) investigated the close association of hyalophane, K-feldspar, and quartz in the phosphate nodules and black shales of Niutitang Formation at Rongxi section, and suggested that K-feldspar may have been largely replaced by hydrothermal Ba^{2+} with the following reaction: $2KAlSi_3O_8$ (K-feldspar) + Ba^{2+} = (K, Ba)$Al_2Si_2O_8$ (hyalophane) + 2 K^+ + $4SiO_2$. Such an association of hyalophane, K-feldspar, and quartz were also observed in the present study and the K-feldspar is surrounded by hyalophane (Fig. 3b and c). Besides, the barite ores at Dahebian section were generally ascribed to Ba-rich hydrothermal activity and the hyalophane-containing barite was widely distributed in these ore deposits (Han et al., 2015). Similarly, hyalophane-containing barite was also clearly identified in our samples (Fig. 3d and e), suggesting Ba-rich hydrothermal activity. Therefore all these observations indicate that the origin of hyalophane is most likely related to the invasion of Ba-rich hydrothermal fluids to black shales and subsequent reactions between Ba-rich fluids and K-feldspar.

The concentrations of Ba_{XS} in the lower unit of the GMD-1 well range from 4267 to 76,679 ppm, with an average value of 21,984 ppm, and these values are 5–100 times higher than that of PAAS (650 ppm) and notably exceed the average value of 4495 ppm for samples from the upper unit. This suggested that the hydrothermal fluids became more Ba-enriched over time during the deposition of the lower and middle units and then gradually weakened or disappeared during the deposition of the upper unit in the shelf region. In contrast, no hyalophane was identified in the TX-1 well, and their concentrations of Ba_{XS} (3679 ppm on average) were also lower than those of the GMD-1 well, suggesting no hydrothermal fluid activity in the slope region.

5.3.2. *Insights from positive Eu anomalies*

Early studies illustrated that hydrothermal activity may also be indicated by positive Eu anomalies (Barrett et al., 1990; Douville et al., 1999; Graf, 1977; Steiner et al., 2001). Eu anomalies have been reported for the Ediacaran–Cambrian black shales in Guizhou and Hunan provinces and invoked for evidence of hydrothermal input (Chen et al., 2006; Chen et al., 2009; Gao et al., 2018; S.Y. Jiang et al., 2007a; Li et al., 2015; Steiner et al., 2001; Wang et al., 2012). At the Dahebian section, stronger positive Eu anomalies are present in barite ore samples (3.2–8.4) than in other shale samples (1.1–1.4), indicating strong hydrothermal activity during the formation of barite ore (Han et al., 2015) (Fig. 8g and h). For the GMD-1 well, positive Eu anomalies are present in all samples and range from 2.2–15.9 in the lower unit through 7.9–9.6 in the middle unit to 1.7–4.1 in the upper unit (Fig. 8a, c, and e). These strongly positive Eu anomalies in the lower and middle units are comparable to those of barite ore samples at the Dahebian section, indicating strong hydrothermal activities during the formation of black shales in the shelf region. In addition, positive Eu anomalies of the upper unit are obviously lower than those of the lower unit, indicating

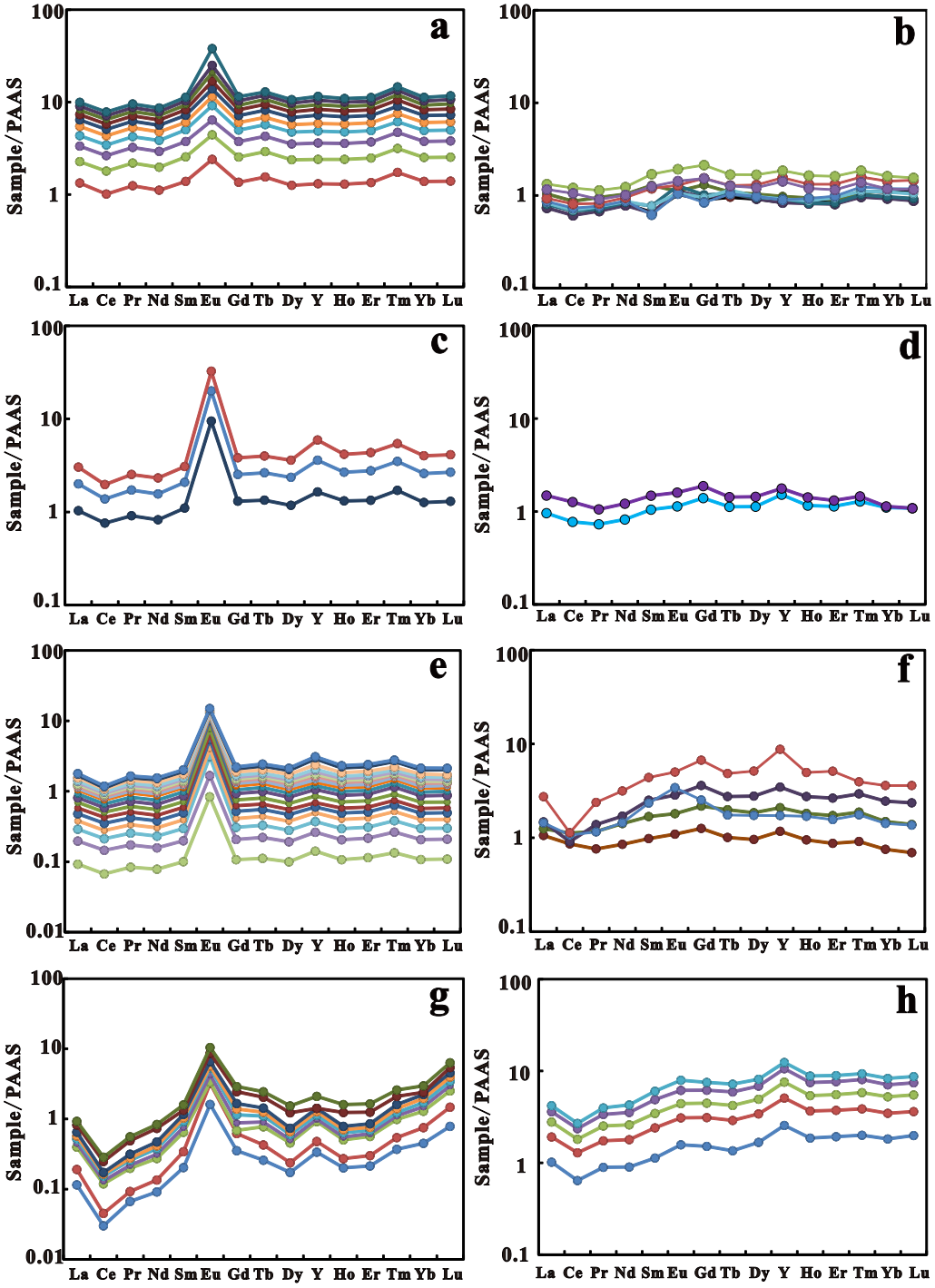

Fig. 8. PAAS-normalized rare earth element compositions of samples analyzed in this study. a: The upper unit of GMD-1well; b: the upper unit of TX-1 well; c: the middle unit of GMD-1 well; d: the middle unit of TX-1 well; e: the lower unit of GMD-1 well; f: the lower unit of TX-1 well; g: barite ores of Dahebian section (Han et al., 2015); h: black shales of Dahebian section (Han et al., 2015).

weakening hydrothermal activity during the deposition of the upper unit. In contrast, only minor Eu anomalies of 0.9–1.5 (on average 1.1) are present in the TX-1 well (Fig. 8b, d, and f), indicating no or minor hydrothermal activity in the slope region.

It is worth noting that care must be taken in the interpretation of Eu anomalies measured by ICP-MS due to interference of various Ba-containing compounds (Dulski, 1994). Such an interference may be evidenced by the positive correlation between Eu/Eu* and Ba_{XS} ($r = +0.88$, $P(\alpha) < 0.01$, $n = 31$) (Fig. 13). However, a close examination of the red rectangular dotted line of Fig. 13 reveals that in the range of Ba_{XS} concentrations of 4000–14,000 ppm, Eu/Eu* ratios in the TX-1 well vary between 0.9 and 1.5 (1.0 on average), showing no obvious anomalies; however, considerably high Eu/Eu* ratios of 1.7–4.1 (3.3 on average) are present in samples from the GMD-1 well. This comparison illustrates that although Eu/Eu* ratios may be influenced by Ba-containing compounds, the strongly positive Eu anomalies observed for the GMD-1 well are indeed related to the hydrothermal activities in the shelf region.

In summary, except for the slope region, there were strong Ba-enriched hydrothermal activities in the regions of the shelf and deep basin

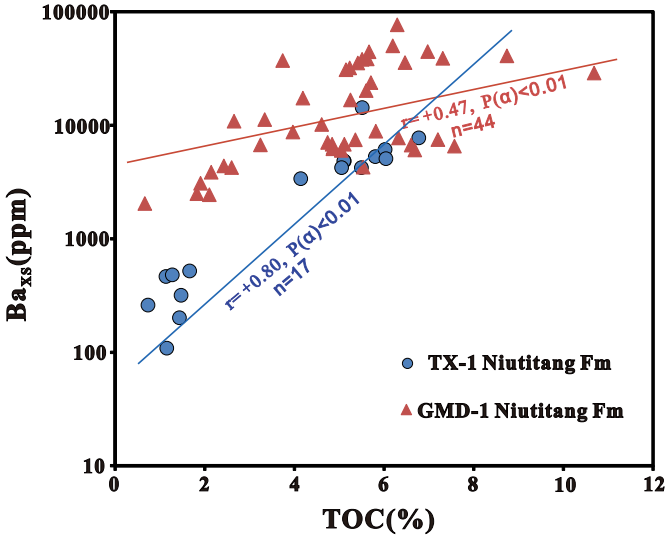

Fig. 9. Cross plot of TOC versus Ba_{XS} for GMD-1 well and TX-1 well samples.

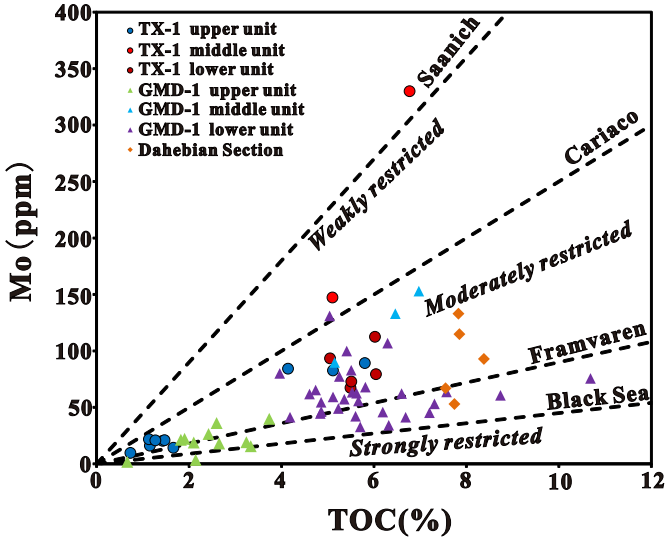

Fig. 10. Cross plot of Mo concentration versus TOC. Dashed lines represent the regression trends for four modern anoxic marine systems (Saanich Inlet, Cariaco Basin, Framvaren Fjord, and Black sea), indicating variable degrees of hydrographic restriction (Algeo and Lyons, 2006).

during the deposition of the lower and middle units (Stage 2 to middle Stage 3), and the hydrothermal activities gradually weakened or disappeared during the deposition of the upper unit (late Stage 3).

5.4. Paleo-environmental model and OM enrichment

The three units of two wells reflect various oceanographic conditions from shelf to slope facies during the early Cambrian, including Stage 2 to early Stage 3, middle Stage 3, and late Stage 3. Organic matter enrichment in these sediments, especially in the lower unit, likely reflects the interaction of multiple factors, including redox conditions, upwelling events and submarine hydrothermal activity. Based on the results of redox conditions from earlier sections on the Yangtze Platform during Cambrian Stage 3, including Xiaotan section in inner shelf (Och et al., 2013), Weng'an section in outer shelf (Jin et al., 2016; Y. Zhang et al., 2017), Songtao section in the slope region (Feng et al., 2014), and Dahebian section in the basin (Han et al., 2015) and the present results of productivity, redox conditions, hydrothermal activity, an integrated environmental and organic matter enrichment model

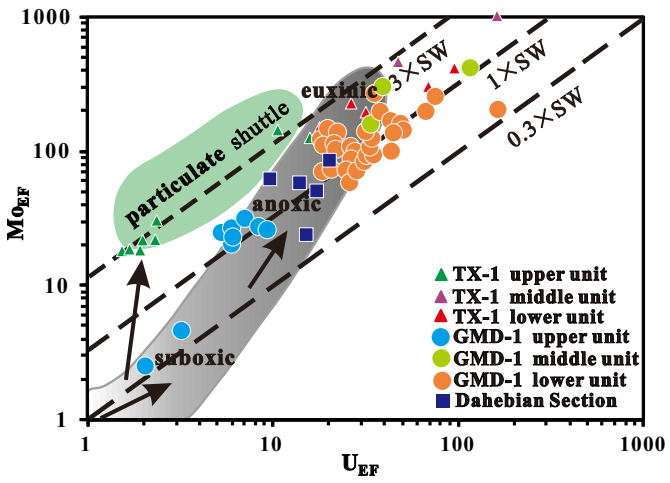

Fig. 11. Plot of Mo_{EF} versus U_{EF} for GMD-1, TX-1 wells and Dahebian section samples. The diagonal dotted lines represent different Mo:U ratios of modern seawater (0.3, 1, and 3). The gray field represents the "unrestricted marine" trend from suboxic to euxinic regions, whereas the green field represents the "particulate shuttle" trend. (For interpretation of the references to color in this figure legend, the reader is referred to the web version of this article.) (Modified from Algeo and Tribovillard (2009).)

from shelf to slope facies during Stage 3 is established for the study area (Fig. 14).

5.4.1. Stage 2 and early Stage 3 (deposition of the lower unit)

On the restricted carbonate platform of the Yangtze Block, Dengying dolomites were deposited under shallow water and oxic environments during the E-C transition. With the rapid rise of sea level during Fortunian and Stage 2, the sedimentary environment changed from oxic to anoxic in the study area (Jiang et al., 2009), and a sequence of black shales with chert and phosphorus nodules was deposited. In the slope region, the cherts in the Liuchapo Formation were deposited under relatively deep water during the E-C transition, and the sea level rise further deepened the water depth and strengthened the anoxia of waters in this region, finally forming a lithologic sequence of organic-rich shales with phosphorus nodules. Modern marine phosphorites and phosphate nodules deposits are commonly present in the continental shelf regions and ascribed to upwelling event along the shelf transect, such as the Gulf of California, Chile, Peru, and Namibia (Baturin, 1982; Froelich et al., 1988; Föllmi, 1996). Similarly, widespread phosphorites and phosphate nodule deposits were also developed at the base of Niutitang Formation in the wells GMD-1 and TX-1 (Fig. 3p–r) and at other sections such as Zhongnanchun, Bahuang and Rongxi (D. Chen et al., 2015; Gao et al., 2018; Jiang et al., 2009; Pi et al., 2013), indicating the existence of upwelling event on the Yangtze Platform during the early Cambrian. Yeasmin et al. (2017) also proposed that there were upwelling events on the Yangtze Platform that were induced by the enhanced trade winds during the early Cambrian based on paleomagnetic data and paleo-geographic setting (Scotese et al., 1999; Golonka, 2007). The upwelling events, which may bring basinal nutrient-rich waters into shallow shelf, could have stimulated the prosperity of photosynthetic phytoplankton and enhanced the primary productivity in the surface water, thus promoting organic matter enrichment and burial in the relatively shallow marginal shelf and slope regions (Chen et al., 2009; Coale et al., 1996; Resing et al., 2015; Yeasmin et al., 2017). In addition, during the latest Stage 2, the wide range of sulfur isotopes from Ni-Mo sulfide ores at the base of Niutitang Formation can be interpreted as biologically mediated fractionation due to bacterial sulfate reduction (BSR) in anoxic water columns, producing a large volume of H_2S and forming sulfidic waters (Feng et al., 2014; Lott et al., 1999; Murowchick et al., 1994). At the same time, submarine

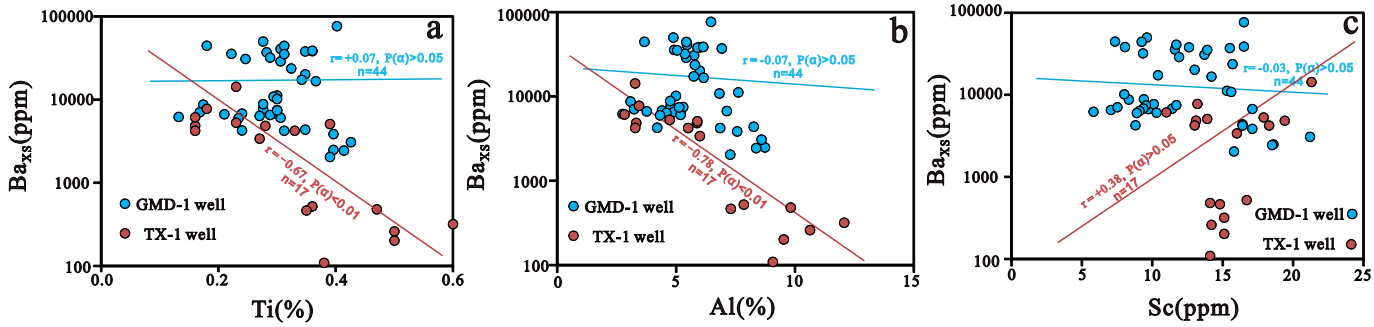

Fig. 12. Plot of Ba_{XS} versus typical elements of terrestrial inputs (Ti, Al, and Sc) for samples from the GMD-1 and TX-1 wells.

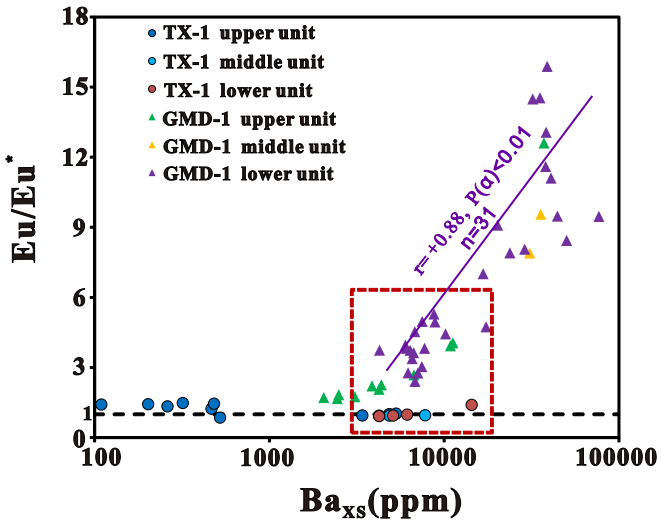

Fig. 13. Plot of Eu/Eu* versus Ba_{XS} for GMD-1 well and TX-1 well core samples.

hydrothermal activities might vent both metal ions such as Ba^{2+}, Ni^{2+}, Fe^{2+} and As^{3+} besides H_2S (Gao et al., 2016; Och et al., 2013). Subsequently, the exposure of metallic ions to H_2S contributes to the formation of sulfidized organic compounds (MoSC phase) and metallic sulfide minerals such as millerite, gersdorffite and sphalerite (Xu et al., 2013). Finally, a wide distribution of the Ni-Mo-PGE-Au sulfide ore layer formed on the Yangtze carbonate platform (Feng et al., 2014; Lehmann et al., 2007; Lott et al., 1999; Och et al., 2013; Steiner et al., 2001; Xu et al., 2013).

Subsequently, the sedimentary environments changed from sulfidic to anoxic waters with occasional euxinic waters during early Stage 3, which is evidenced by the redox indices of the lower unit of Niutitang shales. At the same time, Ba-rich hydrothermal activities occurred in the shelf and basin regions, as shown by the concentrations of Ba_{XS}, hyalophane and positive Eu anomalies. Based on the investigation of hydrothermal activity and activity intensity of organisms in modern hydrothermal active Fiji basin, Halbach et al. (2001) proposed that the closer to the hydrothermal active area, the higher the intensity of biological activity, and the organism activity intensity in the surface waters could be 1–3 orders of magnitude higher than other ordinary modern ocean. McKibben et al. (1990) and Korzhinsky et al. (1994) also considered that hydrothermal activity was commonly accompanied by the release of bio-limiting nutrients, including N, P, Si, Fe, and Zn, which can significantly enhance marine primary productivity in the photic zone. In South China, the black chert successions and Ni-Mo sulfidic layer on the Yangtze Platform were formed mainly due to hydrothermal venting of Si, Ni, Ba, Fe, and Zn during the early Cambrian, which, at the same time, may also carry a large amount of other nutrients necessary for marine life (Chen et al., 2009; Gao et al., 2016; Jiang et al., 2007a; S.Y. Jiang et al., 2007a; Liu et al., 2015). In this study, the Ba-rich hydrothermal fluid venting along with deep-seated faults in the shelf and basinal regions might result in nutrient-rich bottom waters during early Stage 3. In addition, significant upwelling events brought the nutrient-rich bottom waters, likely aided by the concurrent basinal submarine hydrothermal fluids containing Ba, Ni, Zn, Cu and so on, into the surface waters in the shelf and transitional slope regions (Fig. 14a). Therefore, the productivity of surface water is greatly improved in this period.

The TOC values from the lower unit of the GMD-1 well (3.9–10.7%) and the Weng'an Section (6.1–9.8%) in the shelf region are relatively higher than those from the lower unit of the TX-1 well (5.1–6.8%) in the slope region (Fig. 14a). Since anoxic water conditions are widespread from the shelf to slope regions, this difference in TOC contents may be ascribed to higher primary productivity in the shelf region driven by coastal upwelling and hydrothermal activity. Therefore, it is the primary productivity instead of redox that controlled the organic enrichment during this period. It is worth noting that the TOC values of Songtao Section in the slope region (6.2–11.8%) are highest due to the presence of sulfidic-dominated water (Feng et al., 2014), indicating that high primary productivity and sulfidic water might jointly control the OM enrichment in this area.

5.4.2. Middle Stage 3 (deposition of the middle unit)

During the deposition of the middle unit, the sea level remained high but a gradual increase in oceanic oxygen levels might have appeared (X. Chen et al., 2015; Cheng et al., 2017; Jin et al., 2016; Li et al., 2017). A decrease in the area of wide anoxic waters and enlargement of oxic waters may occur from the shallow shelf to slope setting during this time. For the moderately restricted outer shelf where the GMD-1 well is located, high productivity in the surface water could have gradually led to anoxic conditions in the bottom water caused by aerobic degradation of OM in the process of its passage to the sea floor (Demaison and Moore, 1980). Anoxic/euxinic water conditions might only occur in the locally restricted bottom water, while oxic water conditions spread throughout other regions of the shallow shelf (Fig. 14b). For the TX-1 well in the upper slope region, the area of anoxic water was reduced and the interface of chemocline deepened, and anoxic water might have existed where TX-1 is located as well as in the deep water lower slope and basinal regions (Fig. 14b). The TOC values from the middle unit of the GMD-1 well in the shelf region (5.2–6.9%) are similar to those from the middle unit of the TX-1 well in the slope region (5.1–6.8%) (Fig. 14b). The local anoxic water condition, which was beneficial to the preservation of organic matter, was responsible for OM enrichment during this period.

5.4.3. Late Stage 3 (deposition of the upper unit)

The sea level began to fall slowly, and oceanic oxygen levels continued to increase during late Stage 3 (Y. Zhang et al., 2017). Widespread oxic waters with occasional anoxic waters occurred from the shallow shelf to deep water slope regions, as shown by the redox indices from the upper units, and gave rise to a sequence of interbedded shales

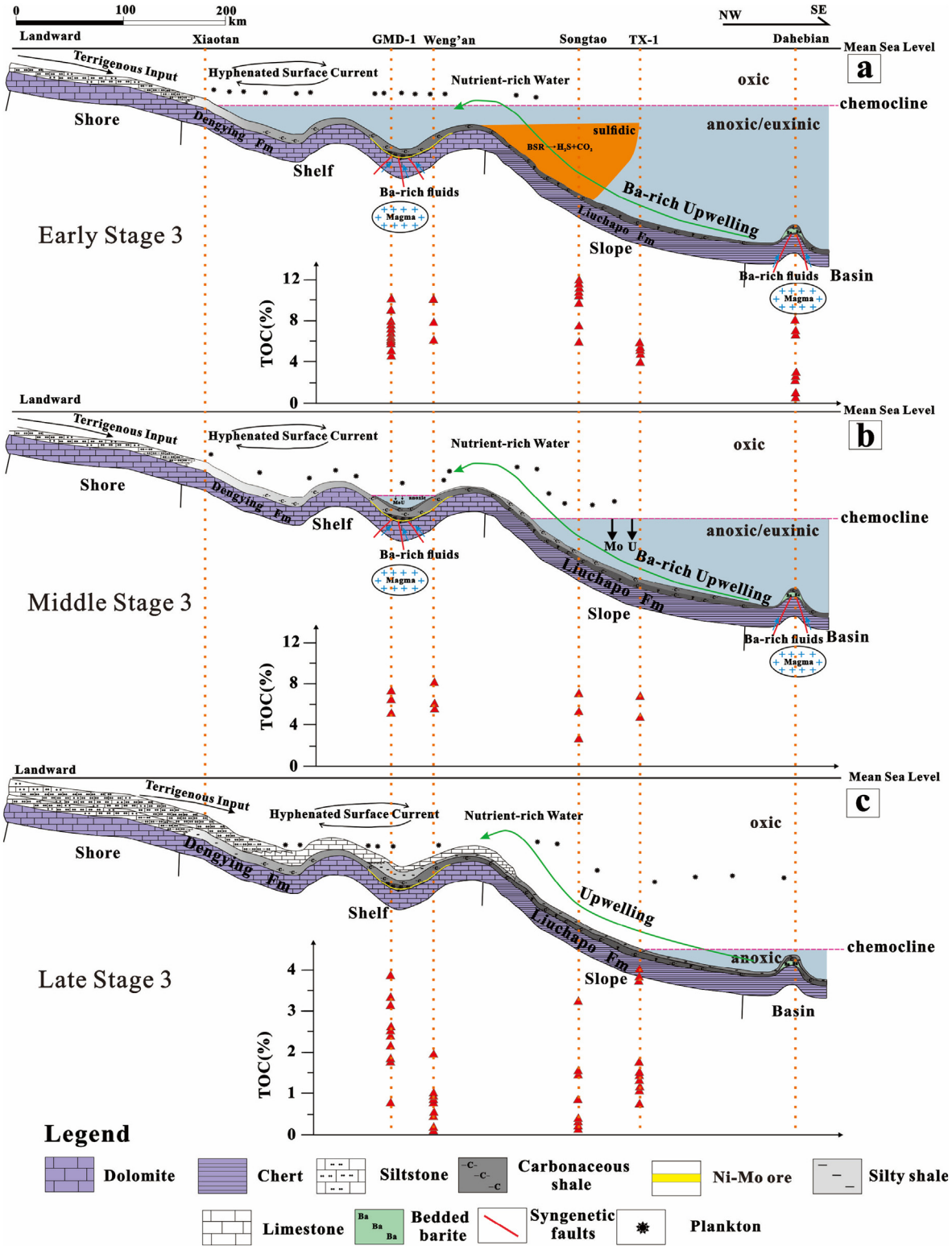

Fig. 14. A model illustrating the Early Cambrian marine redox stratification, distribution of organic-rich shale and spatial variation of TOC in the Yangtze Block during (a) Stage 2 and early Stage 3, (b) middle Stage 3 and (c) late Stage 3. The results of redox conditions from earlier sections include Xiaotan section in inner shelf (Och et al., 2013), Weng'an section in outer shelf (Jin et al., 2016; Y. Zhang et al., 2017), Songtao section in the slope region (Feng et al., 2014), and Dahebian section in the basin (Han et al., 2015). The TOC values of Weng'an and Songtao sections are from Y. Zhang et al. (2017), and Dahebian section are from Han et al. (2015).

and silty shales (Fig. 14c). The Ba-enriched hydrothermal activity gradually weakened or ceased, and the primary productivity also decreased as indicated by the reduced Ba_{XS} content and P/Al ($\times 10^{-4}$) ratios. The TOC values of the upper unit samples of both wells (0.7–5.1%) were lower compared to those of the lower and middle units, and therefore the primary productivity and redox conditions became equally important for OM enrichment in this period.

6. Conclusions

Based on the present geochemical proxies and early studies, widespread anoxic/euxinic water with intermittent sulfidic water columns might be formed from the shallow shelf to deep water slope and basinal regions during Stage 2 and early Stage 3. Then, a decrease in the area of wide anoxic water and an enlargement of oxic water occurred during middle Stage 3, after which fluctuating suboxic and oxic (even occasional anoxic) water conditions predominated during late Stage 3. Strong Ba-enriched hydrothermal activities in the shelf and basin regions occurred during Stage 2 to middle Stage 3 but they gradually weakened or disappeared during late Stage 3; by contrast, no obvious hydrothermal activity is identified in the slope region at the time. The Ba-rich hydrothermal activity and subsequent upwelling event enhanced the primary productivity in surface water and thus promoted OM enrichment. During Stage 2 and early Stage 3, the high primary productivity driven by coastal upwelling and hydrothermal activity were the main factors controlling OM enrichment; during middle Stage 3, the local anoxic water condition became responsible for OM enrichment when oxic waters began to gradually expand; during late Stage 3, both primary productivity and redox conditions became the main control factors for OM enrichment.

Declaration of competing interest

We declare no conflicts of interest, and this manuscript has not been published elsewhere in part or in entirety and is also not under consideration by another journal.

Acknowledgments

The authors are grateful to Prof. Thomas Algeo and two anonymous reviewers for their constructive comments and suggestions that greatly improved the whole quality of the manuscript. This study was jointly supported by Natural Science Foundation of China (Grant No. 41925014 and 41522302) and the National Science and Technology Major Project (2017zx05008-002-004). This is contribution No. IS 2814 from GIGCAS.

References

Algeo, T.J., Lyons, T.W., 2006. Mo-total organic carbon covariation in modern anoxic marine environments: implications for analysis of paleoredox and paleohydrographic conditions. Paleoceanography 21 (1), 1–23.
Algeo, T.J., Maynard, J.B., 2004. Trace-element behavior and redox facies in core shales of Upper Pennsylvanian Kansas-type cyclothems. Chem. Geol. 206 (3), 289–318.
Algeo, T.J., Rowe, H., 2012. Paleoceanographic applications of trace-metal concentration data. Chem. Geol. 324, 6–18.
Algeo, T.J., Tribovillard, N., 2009. Environmental analysis of paleoceanographic systems based on molybdenum-uranium covariation. Chem. Geol. 268 (3), 211–225.
Algeo, T.J., Kuwahara, K., Sano, H., Bates, S., Lyons, T., Elswick, E., Hinnov, L., Ellwood, B., Moser, J., Maynard, J.B., 2011. Spatial variation in sediment fluxes, redox conditions, and productivity in the Permian-Triassic Panthalassic Ocean. Palaeogeogr. Palaeoclimatol. Palaeoecol. 308 (1), 65–83.
Amthor, J.E., Grotzinger, J.P., Schroder, S., Bowring, S.A., Ramezani, J., Martin, M.W., Matter, A., 2003. Extinction of Cloudina and Namacalathus at the Precambrian-Cambrian boundary in Oman. Geology 31 (5), 431–434.
Babcock, L.E., Peng, S., Geyef, G., Shergold, J.H., 2005. Changing perspectives on Cambrian chronostratigraphy and progress toward subdivision of the Cambrian System. Geosci. J. 9, 101–106.
Barrett, T.J., Jarvis, I., Jarvis, K.E., 1990. Rare earth element geochemistry of massive sulfides-sulfates and gossans on the Southern Explorer Ridge. Geology 18 (7), 583–586.
Baturin, G.N., 1982. Phosphorites on the sea floor. In: Developments in Sedimentology, vol. 33. Elsevier, Amsterdam, pp. 343.
Calvert, S.E., Pedersen, T.F., 1993. Geochemistry of recent oxic and anoxic marine sediments-implication for the geological record. Mar. Geol. 113 (1–2), 67–88.
Canfield, D.E., Poulton, S.W., Narbonne, G.M., 2007. Late-Neoproterozoic deep-ocean oxygenation and the rise of animal life. Science 315, 92–95.
Canfield, D.E., Poulton, S.W., Knoll, A.H., Narbonne, G.M., Ross, G., Goldberg, T., Strauss, H., 2008. Ferruginous conditions dominated later Neoproterozoic deep-water chemistry. Science 321, 949–952.
Chen, D., Qing, H., Yan, X., Li, H., 2006. Hydrothermal venting and basin evolution (Devonian, South China): constraints from rare earth element geochemistry of chert. Sediment. Geol. 183 (3–4), 203–216.
Chen, D., Wang, J., Qing, H., Yan, D., Li, R., 2009. Hydrothermal venting activities in the Early Cambrian, South China: petrological, geochronological and stable isotopic constraints. Chem. Geol. 258 (3–4), 168–181.
Chen, D., Zhou, X., Fu, Y., Wang, J., Yan, D., 2015a. New U-Pb zircon ages of the Ediacaran-Cambrian boundary strata in South China. Terra Nova 27 (1), 62–68.
Chen, X., Ling, H.F., Vance, D., Shields-Zhou, G.A., Zhu, M., Poulton, S.W., Och, L.M., Jiang, S.Y., Li, D., Cremonese, L., Archer, C., 2015b. Rise to modern levels of ocean oxygenation coincided with the Cambrian radiation of animals. Nat. Commun. 6, 7142.
Cheng, M., Li, C., Zhou, L., Feng, L., Algeo, T.J., Zhang, F., Romaniello, S., Jin, C., Ling, H., Jiang, S.Y., 2017. Transient deep-water oxygenation in the early Cambrian Nanhua Basin, South China. Geochim. Cosmochim. Acta 210, 42–58.
Coale, K.H., Fitzwater, S.E., Gordon, R.M., Johnson, K.S., Barber, R.T., 1996. Control of community growth and export production by upwelled iron in the equatorial Pacific Ocean. Nature 379, 621–624.
Demaison, G.J., Moore, G.T., 1980. Anoxic environments and oil source bed genesis. Am. Assoc. Pet. Geol. Bull. 64 (8), 1179–1209.
Douville, E., Bienvenu, P., Charlou, J.L., Donval, J.P., Fouquet, Y., Appriou, P., Gamo, T., 1999. Yttrium and rare earth elements in fluids from various deep-sea hydrothermal systems. Geochim. Cosmochim. Acta 63 (5), 627–643.
Dulski, P., 1994. Interferences of oxide, hydroxide and chloride analyte species in the determination of rare earth elements in geological samples by inductively coupled plasma-mass spectrometry. Fresenius J. Anal. Chem. 350 (4), 194–203.
Essene, E.J., Claflin, C.L., Giorgetti, G., Mata, P.M., Peacor, D.R., Arkai, P., Rathmell, M.A., 2005. Two-, three- and four-feldspar assemblages with hyalophane and celsian: implications for phase equilibria in $BaAl_2Si_2O_8$-$CaAl_2Si_2O_8$-$NaAlSi_3O_8$-$KAlSi_3O_8$. Eur. J. Mineral. 17 (4), 515–535.
Feng, L., Li, C., Huang, J., Chang, H., Chu, X., 2014. A sulfate control on marine mid-depth euxinia on the early Cambrian (ca. 529–521Ma) Yangtze platform, South China. Precambrian Res. 246, 123–133.
Fike, D.A., Grotzinger, J.P., Pratt, L.M., Summons, R.E., 2006. Oxidation of the Ediacaran ocean. Nature 444 (7120), 744–747.
Föllmi, K.B., 1996. The phosphorus cycle, phosphogenesis and marine phosphate-rich deposits. Earth Sci. Rev. 40, 55–124.
Froelich, P.N., Arthur, M.A., Burnett, W.C., Deakin, M., Hensley, V., Jahnke, R., Kaul, L., Kim, K.-H., Roe, K., Soutar, A., Vathakanon, C., 1988. Early diagenesis of organic matter in Peru continental margin sediments: phosphorite precipitation. Mar. Geol. 80, 309–343.
Frondel, C., Ito, J., Hendricks, J.G., 1966. Barium feldspars from franklin in newjersey. Am. Mineral. 51 (9), 1388–1393.
Gao, P., Liu, G., Jia, C., Young, A., Wang, Z., Wang, T., Zhang, P., Wang, D., 2016. Redox variations and organic matter accumulation on the Yangtze carbonate platform during Late Ediacaran–Early Cambrian: constraints from petrology and geochemistry. Palaeogeogr. Palaeoclimatol. Palaeoecol. 450, 91–110.
Gao, P., He, Z., Li, S., Lash, G.G., Li, B., Huang, B., Yan, D., 2018. Volcanic and hydrothermal activities recorded in phosphate nodules from the Lower Cambrian Niutitang Formation black shales in South China. Palaeogeogr. Palaeoclimatol. Palaeoecol. 505, 381–397.
Goldberg, T., Strauss, H., Guo, Q., Liu, C., 2007. Reconstructing marine redox conditions for the early Cambrian Yangtze Platform: evidence from biogenic sulphur and organic carbon isotopes. Palaeogeogr. Palaeoclimatol. Palaeoecol. 254, 175–193.
Golonka, J., 2007. Phanerozoic paleoenvironment and plaeolithofacies maps: Early Paleozoic. Geologia 35 (4), 589–654.
Graf, J.L., 1977. Rare-earth elements as hydrothermal traces during formation of massive sulfide deposits in volcanic-rocks. Econ. Geol. 72, 527–548.
Guo, Q., Shields, G.A., Liu, C., Strauss, H., Zhu, M., Pi, D., Goldberg, T., Yang, X., 2007. Trace element chemostratigraphy of two Ediacaran-Cambrian successions in South China: implications for organosedimentary metal enrichment and silicification in the early Cambrian. Palaeogeogr. Palaeoclimatol. Palaeoecol. 254, 194–216.
Halbach, M., Koschinsky, A., Halbach, P., 2001. Report on the discovery of gallionella ferruginea from an active hydrothermal field in the deep sea. Inter Ridge-Crest Res. 10 (1), 18–20.
Han, S., Zhang, J., Li, Y., Horsfield, B., Tang, X., Jiang, W., Chen, Q., 2013. Evaluation of Lower Cambrian shale in Northern Guizhou province, South China: implications for shale gas potential. Energy Fuel 27, 2933–2941.
Han, S., Hu, K., Cao, J., Pan, J., Xia, F., Wu, W., 2015. Origin of early Cambrian black-shale-hosted barite deposits in South China: mineralogical and geochemical studies. J. Asian Earth Sci. 106, 79–94.
Hatch, J.R., Leventhal, J.S., 1992. Relationship between inferred redox potential of the depositional environment and geochemistry of the Upper Pennsylvanian (Missourian) Stark Shale Member of the Dennis Limestone, Wabaunsee County, Kansas, U.S.A. Chem. Geol. 99 (1–3), 65–82.
Hou, Z.Q., Khin, Z., Qu, X.M., Ye, Q.T., Yu, J.J., Xu, M.J., Fu, D.M., Yin, X.K., 2001. Origin of the Gacun volcanic-hosted massive sulfide deposit in Sichuan, China: fluid inclusion and oxygen isotope evidence. Econ. Geol. Bull. Soc. Econ. Geol. 96 (7), 1491–1512.
Jiang, G., Kaufman, A.J., Christie-Blick, N., Zhang, S., Wu, H., 2007a. Carbon isotope variability across the Ediacaran Yangtze platform in South China: implications for a large surface-to-deep ocean $\delta^{13}C$ gradient. Earth Planet. Sci. Lett. 261, 303–320.
Jiang, S.Y., Pi, D.H., Heubeck, C., Frimmel, H., Liu, Y.P., Deng, H.L., Ling, H.F., Yang, J.H., 2009. Early Cambrian ocean anoxia in South China. Nature 459, E5–E6.
Jiang, S.Y., Yang, J.H., Ling, H.F., Chen, Y.Q., Feng, H.Z., Zhao, K.D., Ni, P., 2007a. Extreme enrichment of polymetallic Ni–Mo–PGE–Au in Lower Cambrian black shales of South China: an Os isotope and PGE geochemical investigation. Palaeogeogr.

Palaeoclimatol. Palaeoecol. 254, 217–228.
Jiang, S.Y., Zhao, H.X., Chen, Y.Q., Yang, T., Yang, J.H., Ling, H.F., 2007b. Trace and rare earth element geochemistry of phosphate nodules from the lower Cambrian black shale sequence in the Mufu Mountain of Nanjing, Jiangsu province, China. Chem. Geol. 244 (3–4), 584–604.
Jin, C., Li, C., Algeo, T.J., Planavsky, N.J., Cui, H., Yang, X., Zhao, Y., Zhang, X., Xie, S., 2016. A highly redox-heterogeneous ocean in South China during the early Cambrian (~529–514 Ma): implications for biota-environment co-evolution. Earth Planet. Sci. Lett. 441, 38–51.
Jones, B., Manning, D.A.C., 1994. Comparison of geochemical indices used for the interpretation of paleoredox conditions in ancient mudstones. Chem. Geol. 111 (1–4), 111–129.
Kimura, H., Watanabe, Y., 2001. Oceanic anoxia at the Precambrian-Cambrian boundary. Geology 29, 995–998.
Knoll, A.H., Carroll, S.B., 1999. Early animal evolution: emerging views from comparative biology and geology. Science 284, 2129–2137.
Korzhinsky, M.A., Tkachenko, S.I., Shmlovich, K.I., 1994. Discovery of a purerhenium mineral at Kudriavy volcano. Nature 369, 51–52.
Kribek, B., Hladikova, J., Zak, K., Bendl, J., Pudilova, M., Uhlik, Z., 1996. Barite-hyalophane sulfidic ores at Rozna, Bohemian Massif, Czech Republic metamorphosed black shale-hosted submarine exhalative mineralization. Econ. Geol. Bull. Soc. Econ. Geol. 91, 14–35.
Lehmann, B., Naegler, T.F., Holland, H.D., Wille, M., Mao, J., Pan, J., Ma, D., Dulski, P., 2007. Highly metalliferous carbonaceous shale and Early Cambrian seawater. Geology 35, 403–406.
Li, Y., Fan, T., Zhang, J., Zhang, J., Wei, X., Hu, X., Zeng, W., Fu, W., 2015. Geochemical changes in the Early Cambrian interval of the Yangtze Platform, South China: implications for hydrothermal influences and paleocean redox conditions. J. Asian Earth Sci. 109, 100–123.
Li, C., Jin, C., Planavsky, N.J., Algeo, T.J., Cheng, M., Yang, X., Zhao, Y., Xie, S., 2017. Coupled oceanic oxygenation and metazoan diversification during the early–middle Cambrian? Geology 45 (8), 743–746.
Li, J., Tang, S., Zhang, S., Xi, Z., Yang, N., Yang, G., Li, L., Li, Y., 2018. Paleo-environmental conditions of the Early Cambrian Niutitang Formation in the Fenggang area, the southwestern margin of the Yangtze Platform, southern China: evidence from major elements, trace elements and other proxies. J. Asian Earth Sci. 159, 81–97.
Liu, J.J., Liu, Z.J., Yan, Y., Dan, Y., Cai, F., Hui, X., 2007. Research on the origin geochemistry and biomarkers of the large-scale barium metallogenic belt in the southern Qinling mountains, China. J. Mineral. Petrol. 27, 39–48 (in Chinese with English abstract).
Liu, Z.H., Zhuang, X.G., Teng, G.E., Xie, X.M., Yin, L.M., Bian, L.Z., Feng, Q.L., Algeo, T.J., 2015. The lower Cambrian Niutitang Formation at Yangtiao (Guizhou, SW China): organic matter enrichment, source rock potential, and hydrothermal influences. J. Pet. Geol. 38 (4), 411–432.
Lott, D.A., Coveney, R.M., Murowchick, J.B., Grauch, R.I., 1999. Sedimentary exhalative nickel-molybdenum ores in south China. Econ. Geol. Bull. Soc. Econ. Geol. 94, 1051–1066.
Marshall, C.R., 2006. Explaining the Cambrian “explosion” of animals. Annu. Rev. Earth Planet. Sci. 34, 355–384.
McKibben, M.A., Williams, A.E., Hall, G.E.M., 1990. Solubility and transport of platinumgroup elements and Au in saline hydrothermal fluids; constraints from geothermal brine data. Econ. Geol. 85 (8), 1926–1934.
McManus, J., Berelson, W.M., Hammond, D.E., Klinkhammer, G.P., 1999. Barium cycling in the North Pacific: implications for the utility of Ba as a paleoproductivity and paleoalkalinity proxy. Paleoceanography 14, 53–61.
Morse, J.W., Luther, G.W., 1999. Chemical influences on trace metal-sulfide interactions in anoxic sediments. Geochim. Cosmochim. Acta 63, 3373–3378.
Murowchick, J.B., Coveney, R.M., Grauch, R.I., Eldridge, C.S., Shelton, K.L., 1994. Cyclic variations of sulfur isotopes in Cambrian stratabound Ni-Mo-PGE-Au ores of southern China. Geochim. Cosmochim. Acta 58, 1813–1823.
Murray, R.W., Leinen, M., 1993. Chemical transport to the seafloor of the equatorial Pacific Ocean across a latitudinal transect at 135° W: tracking sedimentary major, trace, and rare earth element fluxes at the Equator and the Intertropical Convergence Zone. Geochim. Cosmochim. Acta 57, 4141–4163.
Och, L.M., Shields-Zhou, G.A., Poulton, S.W., Manning, C., Thirlwall, M.F., Li, D., Chen, X., Ling, H., Osborn, T., Cremonese, L., 2013. Redox changes in Early Cambrian black shales at Xiaotan section, Yunnan Province, South China. Precambrian Res. 225, 166–189.
Pi, D.H., Liu, C.Q., Shields-Zhou, G.A., Jiang, S.Y., 2013. Trace and rare earth element geochemistry of black shale and kerogen in the early Cambrian Niutitang Formation in Guizhou province, South China: constraints for redox environments and origin of metal enrichments. Precambrian Res. 225, 218–229.
Pi, D.H., Jiang, S.Y., Luo, L., Yang, J.H., Ling, H.F., 2014. Depositional environments for stratiform witherite deposits in the Lower Cambrian black shale sequence of the Yangtze Platform, southern Qinling region, SW China: evidence from redox-sensitive trace element geochemistry. Palaeogeogr. Palaeoclimatol. Palaeoecol. 398, 125–131.
Resing, J.A., Sedwick, P.N., German, C.R., Jenkins, W.J., Moffett, J.W., Sohst, B.M., Tagliabue, A., 2015. Basin-scale transport of hydrothermal dissolved metals across the South Pacific Ocean. Nature 523, 200.
Riegler, T., McClenaghan, S.H., 2017. Authigenic potassic silicates in the Rathdowney Trend, southwest Ireland: new perspectives for ore genesis from petrography of gangue phases in Irish-type carbonate-hosted Zn-Pb deposits. Ore Geol. Rev. 88, 140–155.
Rimmer, S.M., 2004. Geochemical paleoredox indicators in Devonian-Mississippian black shales, central Appalachian basin (USA). Chem. Geol. 206, 373–391.
Schenau, S.J., Reichart, G.J., De Lange, G.J., 2005. Phosphorus burial as a function of paleoproductivity. Geochim. Cosmochim. Acta 69, 919–931.
Schoepfer, S.D., Shen, J., Wei, H., Tyson, R.V., Ingall, E., Algeo, T.J., 2015. Total organic carbon, organic phosphorus, and biogenic barium fluxes as proxies for paleomarine productivity. Earth Sci. Rev. 149, 23–52.
Scotese, C.R., Boucot, A.J., McKerrow, S., 1999. Gondwanan paleogeography and paleoclimatology. J. Afr. Earth Sci. 28, 99–114.
Scott, C., Lyons, T.W., Bekker, A., Shen, Y., Poulton, S.W., Chu, X., Anbar, A.D., 2008. Tracing the stepwise oxygenation of the Proterozoic ocean. Nature 452, 456–459.
Shields, G., Stille, P., 2001. Diagenetic constraints on the use of cerium anomalies as palaeoseawater redox proxies: an isotopic and REE study of Cambrian phosphorites. Chem. Geol. 175, 29–48.
Shu, L., 2012. An analysis of principal features of tectonic evolution in South China Block. Geol. Bull. China 31, 1035–1053 (in Chinese with English abstract).
Steiner, M., Wallis, E., Erdtmann, B.D., Zhao, Y.L., Yang, R.D., 2001. Submarine-hydrothermal exhalative ore layers in black shales from South China and associated fossils-insights into a Lower Cambrian facies and bio-evolution. Palaeogeography, Palaeoclimatology, Palaeoecology 169, 165–191.
Steiner, M., Li, G.X., Qian, Y., Zhu, M.Y., Erdtmann, B.D., 2007. Neoproterozoic to early Cambrian small shelly fossil assemblages and a revised biostratigraphic correlation of the Yangtze Platform (China). Palaeogeogr. Palaeoclimatol. Palaeoecol. 254, 67–99.
Taylor, S.R., McLennan, S.M., 1985. The Continental Crust: Its Composition and Evolution. Blackwell Scientific Publications, Oxford, pp. 311.
Tribovillard, N., Algeo, T.J., Lyons, T., Riboulleau, A., 2006. Trace metals as paleoredox and paleoproductivity proxies: an update. Chem. Geol. 232, 12–32.
Tribovillard, N., Algeo, T.J., Baudin, F., Riboulleau, A., 2012. Analysis of marine environmental conditions based on molybdenum-uranium covariation applications to Mesozoic paleoceanography. Chem. Geol. 324–325, 46–58.
Tyrrell, T., 1999. The relative influences of nitrogen and phosphorus on oceanic primary production. Nature 400, 525–531.
Van der Weijden, C.H., 2002. Pitfalls of normalization of marine geochemical data using a common divisor. Mar. Geol. 184, 167–187.
Wang, J., Li, Z.X., 2003. History of Neoproterozoic rift basins in South China: implications for Rodinia break-up. Precambrian Res. 122, 141–158.
Wang, J., Chen, D., Yan, D., Wei, H., Xiang, L., 2012. Evolution from an anoxic to oxic deep ocean during the Ediacaran–Cambrian transition and implications for bioradiation. Chem. Geol. 306–307, 129–138.
Wang, L., Jiu, K., Zeng, W., Fu, J., Zhao, S., 2013. Characteristics of Lower Cambrian marine black shales and evaluation of shale gas prospective area in Qianbei area, Upper Yangtze region. Acta Petrol. Sin. 29, 3263–3278 (in Chinese with English abstract).
Wang, D., Struck, U., Ling, H.F., Guo, Q.J., Shields-Zhou, G.A., Zhu, M.Y., Yao, S.P., 2015a. Marine redox variations and nitrogen cycle of the early Cambrian southern margin of the Yangtze Platform, South China: evidence from nitrogen and organic carbon isotopes. Precambrian Res. 267, 209–226.
Wang, S., Zou, C., Dong, D., Wang, Y., Li, X., Huang, J., Guan, Q., 2015b. Multiple controls on the paleoenvironment of the Early Cambrian marine black shales in the Sichuan Basin, SW China: geochemical and organic carbon isotopic evidence. Mar. Pet. Geol. 66, 660–672.
Wei, H., Chen, D., Wang, J., Yu, H., Tucker, M.E., 2012. Organic accumulation in the lower Chihsia Formation (Middle Permian) of South China: constraints from pyrite morphology and multiple geochemical proxies. Palaeogeogr. Palaeoclimatol. Palaeoecol. 353, 73–86.
Wille, M., Naegler, T.F., Lehmann, B., Schroeder, S., Kramers, J.D., 2008. Hydrogen sulphide release to surface waters at the Precambrian/Cambrian boundary. Nature 453, 767–769.
Xia, F., Dong-Sheng, M.A., Pan, J.Y., Sun, Z.X., Cao, S.L., Chen, S.H., Nie, W.M., Kai, W.U., 2005. Lead isotope geochemistry and lead source of the Dahebian barite deposits, Guizhou Province. Geochimica 34 (5), 501–507 (in Chinese with English abstract).
Xia, W., Yu, B., Sun, M., 2015. Depositional settings and enrichment mechanism of organic matter of the black shales at the bottom of Niutitang Formation, Lower Cambrian in Southeast Chongqing: a case study from Well Yuke 1. Acta Geol. Sin. (English Edition) 89 (S1), 287.
Xu, L., Lehmann, B., Mao, J., Qu, W., Du, A., 2011. Re-Os age of polymetallic Ni-Mo-PGE-Au mineralization in Early Cambrian black shales of South China-a reassessment. Econ. Geol. 106, 511–522.
Xu, L., Lehmann, B., Mao, J., Nägler, T.F., Neubert, N., Böttcher, M.E., Escher, P., 2012. Mo isotope and trace element patterns of Lower Cambrian black shales in South China: multi-proxy constraints on the paleoenvironment. Chemical Geology 318–319, 45–59.
Xu, L., Lehmann, B., Mao, J., 2013. Seawater contribution to polymetallic Ni–Mo–PGE–Au mineralization in Early Cambrian black shales of South China: evidence from Mo isotope, PGE, trace element, and REE geochemistry. Ore Geol. Rev. 52, 66–84.
Yang, R., Wei, H., Bao, M., Wang, W., Wang, Q., Zhang, X., Liu, L., 2008. Discovery of hydrothermal venting community at the base of Cambrian barite in Guizhou Province, Western China: implication for the Cambrian biological explosion. Prog. Nat. Sci. 18, 65–70.
Yang, X.L., Zhao, Y., Wu, W., Zheng, H., Zhu, Y., 2014. Phragmodictya jinshaensis sp. nov., a hexactinellid dictyosponge from the Cambrian of Jinsha, South China. GFF 136, 309–313.
Yeasmin, R., Chen, D., Fu, Y., Wang, J., Guo, Z., Guo, C., 2017. Climatic-oceanic forcing on the organic accumulation across the shelf during the Early Cambrian (Age 2 through 3) in the mid-upper Yangtze Block, NE Guizhou, South China. J. Asian Earth Sci. 134, 365–386.
Zhang, M., Suddaby, P., Thompson, R.N., Dungan, M.A., 1993. The origin of contrasting zoning patterns in hyalophanefrom olivine leucitites, Northeast China. Mineral. Mag.

57, 565–573.
Zhang, J., Fan, T., Algeo, T.J., Li, Y., Zhang, J., 2016. Paleo-marine environments of the Early Cambrian Yangtze Platform. Palaeogeogr. Palaeoclimatol. Palaeoecol. 443, 66–79.
Zhang, K., Jiang, Z., Yin, L., Gao, Z., Wang, P., Song, Y., Jia, C., Liu, W., Liu, T., Xie, X., Li, Y., 2017a. Controlling functions of hydrothermal activity to shale gas content-taking lower Cambrian in Xiuwu Basin as an example. Mar. Pet. Geol. 85, 177–193.
Zhang, Y., He, Z., Jiang, S., Gao, B., Liu, Z., Han, B., Wang, H., 2017b. Marine redox stratification during the early Cambrian (ca. 529–509 Ma) and its control on the development of organic-rich shales in Yangtze Platform. Geochem. Geophys. Geosyst. 18, 2354–2369.
Zhang, K., Song, Y., Jiang, S., Jiang, Z., Jia, C., Huang, Y., Wen, M., Liu, W., Xie, X., Liu, T., Wang, P., Shan, C., Wu, Y., 2019. Mechanism analysis of organic matter enrichment in different sedimentary backgrounds: a case study of the Lower Cambrian and the Upper Ordovician-Lower Silurian, in Yangtze region. Mar. Pet. Geol. 99, 488–497.
Zhao, Y.L., Yu, Y.Y., Yuan, J.L., Yang, X.L., Guo, Q.J., 2001. Cambrian stratigraphy at Huanglian, Guizhou Province, China: reference section for bases of the Nangaoan and Duyunian stages. Palaeoworld 13, 172–181.
Zhu, M., Zhang, J., Steiner, M.D., Yang, A., Li, G., Erdtmann, B.D., 2003. Sinian Cambrian stratigraphic framwork for shallow- to deep-water environments of the Yangtze Platform: an integrated approach. Prog. Nat. Sci. 13, 951–960.